

Constraining cosmological parameters using void statistics from the SDSS survey

Elena Fernández-García^{1*}, Juan E. Betancort-Rijo^{2,3}, Francisco Prada¹, Tomoaki Ishiyama⁴, and Anatoly Klypin⁵

¹ Instituto de Astrofísica de Andalucía (CSIC), E18008 Granada, Spain,

² Instituto de Astrofísica de Canarias, C/ Via Lactea s/n, Tenerife E38200, Spain

³ Facultad de Física, Universidad de La Laguna, Astrofísico Francisco Sanchez, s/n, La Laguna, Tenerife E38200, Spain

⁴ Digital Transformation Enhancement Council, Chiba University, 1-33, Yayoi-cho, Inage-ku, Chiba, 263-8522, Japan

⁵ Department of Astronomy, University of Virginia, Charlottesville, VA 22904, USA

Received ..., ...; accepted ..., ...

ABSTRACT

Aims. Constraining the values of the amplitude of the linear spectrum of density fluctuations (σ_8), the matter density parameter (Ω_m), the Hubble constant (H_0), $\Gamma = \Omega_c h$, where Ω_c is the dark matter density parameter and $h = H_0/100$, and S_8 from the SDSS survey by studying the abundance of large voids in the large-scale structure of galaxies.

Methods. We identify voids as maximal non-overlapping spheres within the haloes of the Uchuu simulation and three smaller halo simulation boxes with smaller volume and different σ_8 values, and galaxies with redshift in the range $0.02 < z < 0.132$ and absolute magnitude in the r -band $M_r < -20.5$ of 32 Uchuu-SDSS simulated lightcones the seventh release of *The Sloan Digital Sky Survey* (SDSS DR7) survey. We compute the Void Probability Function (i.e. the probability that a randomly placed sphere with radius r is empty of tracers) and the abundance of voids larger than r predicted by the theoretical framework used and improved in this work and we check that it predicts successfully both void functions for the halo simulation boxes. Next, we assess the potential of this theoretical framework to constrain cosmological parameters using Uchuu-SDSS void statistics, and we calculate the confidence levels using Monte Carlo Markov Chain techniques to infer the values of σ_8 , Ω_m and H_0 from the SDSS sample used.

Results. We have proved that using the four halo simulation boxes we successfully recover the values of σ_8 , Ω_m and h from each box within 1σ (2σ) in real (redshift) space. We have also proved that the theoretical framework is really powerful using Uchuu-SDSS void statistics: if we fix one parameter to a constant value, the value given by Planck of the other two parameters is inside the 1σ confidence level contour only if the fixed parameter is close enough to Planck's value. Then, we have constrained these parameters from the SDSS survey sample used. The results are: $\sigma_8 = 1.028^{+0.273}_{-0.305}$, $\Omega_m = 0.296^{+0.110}_{-0.102}$, $H_0 = 83.43 \pm^{+29.27}_{-27.70}$, $\Gamma = 0.1947^{+0.0578}_{-0.0516}$ and $S_8 = 1.017^{+0.363}_{-0.359}$. If we combine these constraints with KiDS-1000+DESY3, we get $\sigma_8 = 0.858^{+0.040}_{-0.040}$, $\Omega_m = 0.257 \pm^{+0.023}_{-0.020}$, $H_0 = 74.17^{+4.66}_{-4.66}$ and $S_8 = 0.794^{+0.016}_{-0.016}$. The combined uncertainties are approximately a factor 2-3 smaller than only-Weak-Lensing uncertainties. This is a consequence of the orientation of the confidence level contours of SDSS voids and Weak Lensing in the plane $\sigma_8 - \Omega_m$, which are almost orthogonal.

Key words. cosmological parameters – large-scale structure of the Universe – cosmic voids – void-statistics – simulations

1. Introduction

For over 40 years, it has been observed that the brightest galaxies are generally found in dense regions, and that most of cosmic space is devoid of this type of galaxies. This distribution is well understood as a natural evolution of density fluctuations in matter that were progressively amplified by gravitational instability (Giovanelli 2010). In this framework, it can be demonstrated that initially low-density regions (voids) grow in size as highly dense areas collapse under their own gravity (Sheth & Van De Weygaert 2004).

In the last century, there has been a significant focus on studying the over-dense regions of the Universe (e.g. Kiang & Saslaw 1969; Bahcall 1977; Kaiser 1987; Einasto et al. 1994; Holder et al. 2001; Yang et al. 2005; Li et al. 2006; Gao & White 2007; Zentner et al. 2019; Dong-Páez et al. 2024), while the under-dense areas have only recently begun to receive adequate attention (e.g. Hoffman & Shaham 1982; Zeldovich et al. 1982; Little & Weinberg 1994; Goldwirth et al. 1995; van de Weygaert & Sheth 2003; Li et al. 2012; Achitouv 2019; Chan et al.

2019; Rodríguez-Medrano et al. 2024; Curtis et al. 2024). Studying these regions (voids) is very useful as they possess unique characteristics that make them important probes for cosmological studies and the physics of galaxy formation. They are useful, for example, for:

- constraining the equation of state of dark energy (e.g. Lee & Park 2009; Biswas et al. 2010; Sutter et al. 2014; Contarini et al. 2022),
- studying modified gravity (e.g. Martino & Sheth 2009; Clampitt et al. 2013; Voivodic et al. 2017; Falck et al. 2017; Perico et al. 2019; Contarini et al. 2021; Mauland et al. 2023)
- constraining cosmological models (e.g. Ryden 1995; Benson et al. 2003; Croton et al. 2005; Lavaux & Wandelt 2010),
- constraining cosmological parameters based on their statistics (e.g. Betancort-Rijo et al. 2009; Nadathur 2016; Hamaus et al. 2020; Aubert et al. 2022; Contarini et al. 2022, 2023),
- testing the primordial non-Gaussianities (e.g. Song & Lee 2009; Chongchitnan & Silk 2010; Chan et al. 2019).

In fact, in principle, any cosmological parameter could be constrained from void statistics. Specifically, the abundance of

* e-mail: efdez@iaa.es

voids with radius larger than r , $N_v(r)$, depends on the normalization of the linear spectrum of density fluctuations (σ_8) and $\Gamma = \Omega_c$, and the shape of this function for large values of r depends on $\Gamma = \Omega_c h$, where $h = H_0/100 \text{ km s}^{-1} \text{ Mpc}^{-1}$ (see [Betancort-Rijo et al. \(2009\)](#) for details).

Constraining σ_8 and $\Gamma = \Omega_c h$ is especially interesting as there exist some statistically significant tension in cosmological parameter $S_8 = \sigma_8 \sqrt{\Omega_m/0.3}$ between the Planck experiment ([Aghanim et al. 2020](#)), which measures the Cosmic Microwave Background, CMB, anisotropies ($S_8 = 0.834 \pm 0.0161$), and other low-redshift cosmological probes, such as weak gravitational lensing, where a value of $S_8 = 0.776^{+0.032}_{-0.030}$ is obtained by KiDS-1000 ([Li et al. 2023](#)). This tension is known as the S_8 tension. (see [Di Valentino et al. \(2021\)](#) for more details).

Initial investigations into cosmic voids were constrained by the limited quantity of surveyed galaxies during that period. Nevertheless, with the emergence of more expansive redshift surveys, such as the Two-Degree Field Galaxy Redshift Survey (2dFGRS) ([Colless et al. 2001, 2003](#)), the Sloan Digital Sky Survey (SDSS) ([York et al. 2000](#)) and The SDSS's Baryon Oscillation Spectroscopic Survey (BOSS) ([Dawson et al. 2013](#)), alongside improved resolution in cosmological simulations and enhanced analytical methodologies, we now have the capability to derive precise statistical insights concerning voids (e.g. [Tikhonov 2006](#); [Ceccarelli et al. 2006](#); [von Benda-Beckmann & Mueller 2007](#); [Tikhonov 2007](#); [Patiri et al. 2012](#); [Hamaus et al. 2020](#); [Douglass et al. 2023](#); [Contarini et al. 2023](#)).

However, despite the longstanding presence of the concept of cosmic voids, there exists no universally accepted definition for what constitutes a void. The term "voids" can encompass disparate entities depending on the data employed and the objectives of the analysis. For example, voids can be defined as under-dense regions based on the smoothed dark matter (or halo/galaxy) density field ([Colberg et al. 2005](#)), as gravitationally expanding regions based on the dynamics of the dark matter density field ([Hoffman et al. 2012](#)), or as empty spatial regions among discrete tracers ([El-Ad & Piran 1997](#); [Aikio & Mähönen 1998](#); [Hoyle & Vogeley 2002](#)).

The choice of a simple definition of voids, in particular, their definition as empty spheres, is convenient for statistical studies of galaxy voids. In this paper, we define voids as maximal non-overlapping spheres empty of objects with mass (or luminosity) above a given value. With this definition, it is clear that voids are not empty, as there can be low luminosity galaxies (or low mass haloes) inside them.

The aim of this paper is to infer the values of σ_8 , H_0 and Ω_m from SDSS redshift survey using the theoretical framework of voids statistics developed in [Betancort-Rijo \(1990\)](#). This has been already done in previous articles in different ways. For example, in [Sahlén et al. \(2016\)](#) galaxy cluster and void abundances are combined using extreme-value statistics on a large cluster and a void. This way they obtain a value of $\sigma_8 = 0.95 \pm 0.21$ for a flat Λ CDM universe. In [Hamaus et al. \(2016\)](#), they constrain $\Omega_m = 0.281 \pm 0.031$ studying void dynamics in SDSS. In [Woodfinden et al. \(2023\)](#) they also use SDSS survey to constrain $\Omega_m = 0.391^{+0.028}_{-0.021}$ measuring the void-galaxy and galaxy-galaxy clustering. In [Contarini et al. \(2023\)](#) they model Void Size Function ([Press & Schechter 1974](#); [Sheth & Van De Weygaert 2004](#)) by means of an extension of the popular volume-conserving model ([Jennings et al. 2013](#)), based on two additional nuisance parameters, and applying a Bayesian analysis they get a value of $\sigma_8 = 0.79^{+0.09}_{-0.08}$ for BOSS DR12, and, in a posterior work ([Contarini et al. 2024](#)), they constrain $S_8 = 0.813^{+0.093}_{-0.068}$ and $H_0 = 67.3^{+10}_{-9.1}$ for the same redshift survey.

This paper is structured as follows: in Section 2 we describe the redshift survey as well as the simulations used in this work. Next, in Section 3 we give a detail explanation of how our Void Finder works and show the relevant statistics of voids obtained for the observational catalogue and compare it with the result of Uchuu-SDSS lightcones. In Section 4 we introduce the most important concepts and equations used in the theoretical framework to calculate the abundance of voids larger than r and the Void Probability Function. We show that the theoretical framework predicts successfully these two void statistics for halo simulation boxes with different σ_8 values in real and redshift space, and show the results for SDSS and the Uchuu-SDSS lightcones. In Section 5 we explain the statistical test we use in order to infer σ_8 , Ω_m and h . In Section 6 we show the potential of the theoretical framework using Uchuu-SDSS void statistics, i.e., we show that if we let two of the three cosmological parameters be free, the third parameter must be very close to Planck's best-fit value in order to recover the real values of other two parameters. In this section, we also show the inferred values of σ_8 , Ω_m , h , Γ and S_8 from Uchuu-SDSS. In Section 7 we show the constrained values for the sample of SDSS redshift survey we have used in this work and we combine our results with KiDS-1000 results ([Dark Energy Survey and Kilo-Degree Survey Collaboration et al. 2023](#)). In Section 8 we compare our constrained values of σ_8 , Ω_m and H_0 with those obtained in other works where voids are also used. Finally, in Section 9 we summarize the most important results obtained in this work.

2. Data and mocks

The aim of this work is to infer σ_8 , Ω_m and H_0 values from *The Sloan Digital Sky Survey*. However, to make sure that the theoretical equations reproduce correctly the void functions of this redshift survey, we also use 4 halo simulation boxes with different σ_8 values (see Table 1), one simulation galaxy box and 32 lightcones. In this section we introduce the redshift survey and mocks.

2.1. SDSS

We have used the seventh release ([Abazajian et al. 2009](#)) of *The Sloan Digital Sky Survey* (SDSS DR7) ([York et al. 2000](#)), which includes 11663 deg^2 of CCD imaging data in 5 photometric bands for 357 million distant objects. The catalogue also completed spectroscopy over 9380 deg^2 . In total, there are 1.6 million spectra, including 930000 galaxies, 120000 quasars, and 460000 stars.

However, in this work we use a subcatalogue of SDSS: only galaxies from the northern regions with completeness greater than 90% are selected. Therefore, the effective area of this subcatalogue is 6511 deg^2 and contains around 497000 galaxies with redshifts between $z \in (0, 0.5)$. In this sample, $\sim 6\%$ of targeted galaxies lack a spectroscopically measured redshift due to fibre collisions, so nearest neighbour correction is applied to these galaxies, assigning to them the redshift of the galaxy with which they collide ([Dong-Páez et al. 2024](#)).

Additionally, we impose further cuts on absolute magnitude and redshift, and we construct a volume-limited sample by keeping only galaxies brighter than the Milky Way-like galaxies ($M < -20.5$, where M_r is the absolute magnitude in r -band) and with $z \geq 0.02$ and $z \leq 0.132$. The physical volume of this sample is $V = 41.67 \times 10^6 h^{-3} \text{ Mpc}^3$. There are in total 112496 galaxies which fulfil these restrictions, so the number density of the galaxies is $n_g = 2.838 \times 10^{-3} h^{-3} \text{ Mpc}^3$.

	Uchuu	P18(Low)	VeryLow
Ω_m	0.3089	0.3111	0.3111
Ω_Λ	0.6911	0.6889	0.6889
Ω_b	0.0486	0.048975	0.048975
h	0.6774	0.6766	0.6766
σ_8	0.8159	0.8102 (0.75)	0.65
$L_{\text{box}} [h^{-1}\text{Mpc}]$	2000	1000	1000
N_{part}	12800 ³	6400 ³	3200 ³
$M_{\text{part}} [h^{-1}M_\odot]$	3.27×10^8	3.29×10^8	2.63×10^9
$\varepsilon [h^{-1}\text{kpc}]$	4.27	1.0	4.0
Haloes	Yes	Yes	Yes
Galaxies	Yes	No	No
Lightcones	Yes (32)	No	No

Table 1: Cosmological parameters (first five rows), the size of the simulation box (L_{box}), the number of dark matter particles used in the simulation (N_{part}), their mass (M_{part}), and the gravitational softening (ε) for Uchuu, Uchuu1000P18 (P18), Uchuu1000P18LowS8 (Low) and Uchuu1000P18VeryLowS8 (VeryLow) used to generate the box catalogs in this work. The last five rows provide information about whether the box catalog, galaxy box or lightcones for SDSS are available for each simulation.

2.2. Mocks

We use the Uchuu simulation, which was produced using the *TreePM* code *Greem* * (Ishiyama et al. 2009, 2012) on the supercomputer ATERUI II at Center for Computational Astrophysics, CfCA, of National Astronomical Observatory of Japan. The number of dark matter particles was 12800³ with a mass resolution of $3.27 \times 10^8 h^{-1} M_\odot$ in a box with a side length of 2000 h^{-1} Mpc. A total of 50 halo catalogs (*snapshots*) were created, covering the redshift range from 0 to 14 (Ishiyama et al. 2021). The haloes were subsequently identified using the *RockStar* halo/subhalo finder † (Behroozi et al. 2013a), and merger trees were generated using the consistent trees code ‡ (Behroozi et al. 2013b). These simulations adopted the cosmological parameters from Planck 2015 (see Table 1) (Planck Collaboration et al. 2016). All this data is publicly available and accessible in the *Skies & Universes* database §, including galaxy catalogs constructed using various methods (Aung et al. 2023; Oogi et al. 2023; Gkogkou et al. 2023; Prada et al. 2023; Ereza et al. 2023; Dong-Páez et al. 2024).

Apart from Uchuu, we use three more simulations with Planck 2018 (Aghanim et al. 2020) (Uchuu1000P18), Planck 2018 with $\sigma_8 = 0.75$ (Uchuu1000P18LowS8) and Planck 2018 with $\sigma_8 = 0.65$ (Uchuu1000P18VeryLowS8). Uchuu1000P18 and Uchuu1000P18LowS8 have exactly the same simulation properties, except the value of σ_8 . Uchuu1000P18VeryLowS8 has different value of σ_8 and different mass resolution. All these details can be seen in Table 1. These three simulations were produced using the *TreePM* code *Greem* on the supercomputer Fugaku at the RIKEN Center for Computational Science. As well as the Uchuu simulation, we generated initial conditions for these three simulations with 2nd order Lagrangian perturba-

tion theory (Crocce et al. 2006) by *2LPTIC* code ¶. The initial conditions are identical across the three simulations, enabling us to compare them without cosmic variance. The total of 70 halo catalogs were created, where the redshift list is the same with the Uchuu at $z < 6$. N-body data including the halo catalogs and the merger trees are also available in the *Skies & Universes* database.

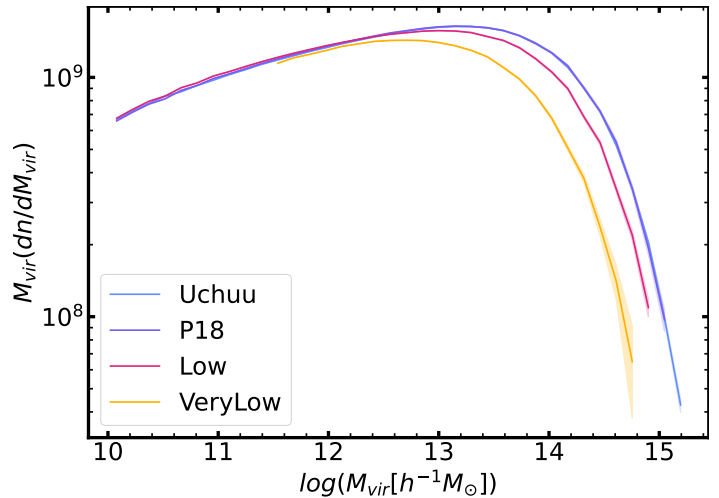


Fig. 1: Halo Mass Function multiplied by the mean halo mass within virial radius (including unbound particles) of each bin of the four box catalogs used in this work. Shaded regions represent poissonian errors.

The Halo Mass Function (HMF) of each simulation can be seen in Figure 1, where $M_{\text{vir},\text{all}}$ is the halo mass within virial radius including unbound particles. In this figure it can be seen that VeryLow has lower mass resolution, as the HMF decreases considerably for small masses. It is also shown that, specially for large masses, the lower σ_8 is the lower the HMF is too. Additionally, it can be seen that there is no significant difference between P18, Low and VeryLow halo mass functions for low virial masses ($M_{\text{vir},\text{all}} < 10^{12} h^{-1} M_\odot$), but there is a significant difference for large virial masses ($M_{\text{vir},\text{all}} > 10^{12} h^{-1} M_\odot$).

We also use a galaxy simulation box that has been generated from Uchuu simulation using the SubHalo Abundance Matching (SHAM) method. From the galaxy boxes for different *snapshots*, lightcones with the properties of SDSS have been constructed. In concrete, 32 light cones are available. The Uchuu galaxy box and the 32 simulated SDSS light cones we use in this work are extensively detailed in Dong-Páez et al. (2024).

For the purpose of studying void statistics in simulation boxes, we select those *snapshots* corresponding to a redshift of $z \sim 0.092$ (which is the snapshot with the closest redshift to SDSS median redshift). Moreover, we don't use all the objects (haloes or galaxies) from this boxes, but we select a number density of $\bar{n} = 3 \times 10^{-3} h^{-3} \text{Mpc}^3$ for each box. This can be reached removing haloes less massive than $M_{\text{vir},\text{all}} = 1.626 \times 10^{12} M_\odot / h$ (Uchuu), $1.642 \times 10^{12} M_\odot / h$ (Uchuu1000P18), $1.595 \times 10^{12} M_\odot / h$ (Uchuu1000P18LowS8) and $1.457 \times 10^{12} M_\odot / h$ (Uchuu1000P18VeryLowS8), and galaxies less brighter than $M_r < -20.5$ for Uchuu galaxy box.

3. Statistics of voids in the SDSS

The next important step we need to take once we have well-defined the sample of halos or galaxies we are going to use is

¶ <http://cosmo.nyu.edu/roman/2LPT/>

* <http://hpc.imit.chiba-u.jp/~ishiytm/greem/>
 † <https://bitbucket.org/gfcstanford/rockstar/>
 ‡ <https://bitbucket.org/pbehroozi/consistent-trees/>
 § <http://www.skiesanduniverses.org/Simulations/Uchuu/>

to identify voids, defined as maximum non-overlapping spheres. To do this, we perform Delaunay triangulation (with periodic conditions for simulation boxes).

The Delaunay triangulation of a set of points p_i ensures that no point p_i lies within the circumcircle of any triangle in the triangulation. Additionally, Delaunay triangulations maximize the minimum angle among all triangle angles, aiming to reduce the occurrence of sliver triangles.

Fortunately, there is a publicly available code that uses the CGAL (The Computational Geometry Algorithms Library)^{||} for 3D triangulations. This code is called *Delaunay triangulation Void findEr* (DIVE^{**}), which is used and explained in Zhao et al. (2016). The output of this code is a file that contains the positions in space of the centres of the spheres that satisfy the Delaunay condition, as well as their radii. However, these spheres are not voids, but candidates to be voids.

To find voids (i.e. maximal non-overlapping spheres) among these spheres, an additional code needs to be developed. This code must check if two spheres overlap and, in case they do, keep the largest one as a void.

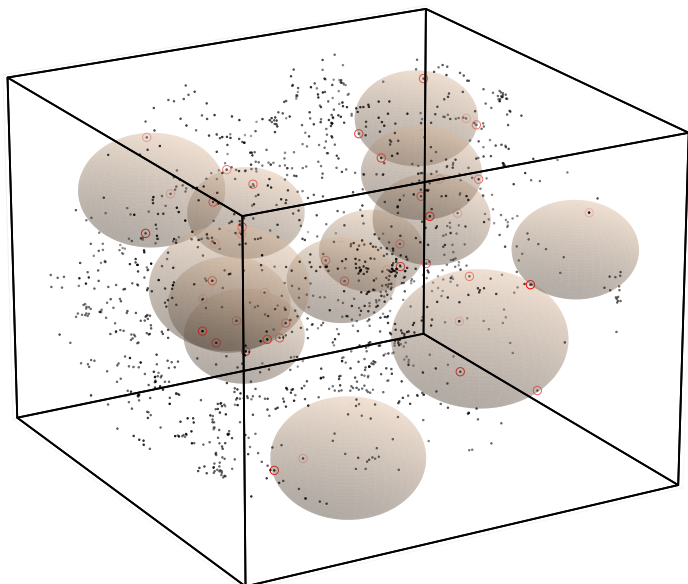


Fig. 2: Voids with $r > 9h^{-1}\text{Mpc}$ (spheres) found in a region of P18 box catalog (black and red points) with number density $3 \times 10^{-3}h^{-3}\text{Mpc}^3$. Points that define the voids (i.e. those lying in their surface) are highlighted with a red circle. The volume of the box is 80^3h^{-3}Mpc^3 .

In Figure 2 the voids larger than $r > 9h^{-1}\text{Mpc}$ found in the P18 halo simulation box with number density $3 \times 10^{-3}h^{-3}\text{Mpc}^3$ are shown in a region of the box. It can be seen that each void is defined by four galaxies laying in its surface (some voids in Figure 2 have fewer than 4 galaxies due to being outside the plotted region), and it is ensured that voids do not overlap.

However, for the galaxy lightcones, one more step is required. This step involves considering the incompleteness in stellar mass, which causes many spurious voids to appear. These spurious voids correspond to regions in the catalog with very low completeness, where galaxies could not be detected properly. Therefore, these *false voids* must be eliminated using an

^{||}<https://doc.cgal.org/4.6.3/Manual/packages.html#PkgTriangulation3Summary>

^{**}<https://github.com/cheng-zhao/DIVE>

angular mask, such as the Healpix map (Gorski et al. 1999; Blanton et al. 2005; Swanson et al. 2008), characteristic of the redshift survey.

The procedure for removing these false voids is as follows: first, we generate points uniformly distributed within the volume of the void. Next, we project these points in the angular plane, calculate the completeness of each point and average the completeness of all points within the void to obtain an approximation of the completeness of the void. If this completeness is equal to or greater than 0.9, we label that void as a true void. Otherwise, we remove the false void.

Additionally, voids whose centers or part of their volume are outside the sample in the radial direction must also be removed, as the procedure explained above considers only the angular plane, but voids may extend beyond the sample in the radial direction, so this extra check is necessary.

r	SDSS	Uchuu-SDSS
10	797 ± 12	792.2 ± 2.1
11	550 ± 15	550 ± 3
12	381 ± 13	366.3 ± 2.3
13	248 ± 13	233.4 ± 2.2
14	150 ± 11	140.6 ± 1.9
15	85 ± 8	78.9 ± 1.4
16	51 ± 7	41.4 ± 1.2
17	27 ± 5	21.2 ± 0.8
18	15 ± 3	9.3 ± 0.5
19	7.0 ± 1.7	3.4 ± 0.3
20	1.0 ± 1.0	0.97 ± 0.18

Table 2: Abundance of voids larger than r , $N_v(r)$, obtained for voids found in the distribution of SDSS (first row) and Uchuu-SDSS (second row) galaxies with $M_r < -20.5$ and $0.02 < z < 0.132$.

In Figure 3 the number density of voids larger than r , $n_v(r)$, obtained for voids found in the sample of SDSS and Uchuu-SDSS (the mean of the 32 lightcones) considered in this work (galaxies with $M_r < -20.5$ and $0.02 < z < 0.132$) are shown (in Table 2 the values are multiplied by the volume). It can be checked that Uchuu-SDSS statistics are compatible with observations for all radius bins, although there are big fluctuations in SDSS that appear for large voids ($r > 16h^{-1}\text{Mpc}$) due to the small volume of the survey.

An important remark about Figure 3 is that if we want to compare the observed number density of voids larger than r obtained from SDSS (or Uchuu-SDSS) with that given by the theoretical framework presented in this work, we must take into account that the former suffers from incompleteness, and other effects such as border effects, and the latter doesn't. Therefore, we have to transform SDSS (and Uchuu-SDSS) void statistics as if it didn't suffer from these effects. One way of doing this is using Uchuu galaxy box. Then, SDSS and Uchuu-SDSS number density of voids larger than r must be transformed as:

$$n_v(r) \rightarrow n_v(r)(Uchuu) \frac{N_v(r)(SDSS)}{N_v(r)(Uchuu - SDSS)} \quad (1)$$

where $N_v(r)(Uchuu - SDSS)$ is the number of voids larger than r found in Uchuu-SDSS lightcones, and $N_v(r)(Uchuu)$ is the same but found in Uchuu galaxy box, and V_{Uchuu} is the volume of Uchuu simulation ($V=2000^3h^{-3}\text{Mpc}^3$).

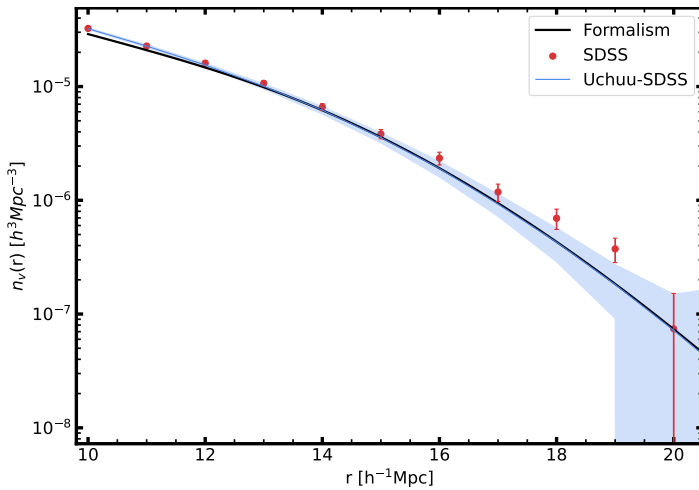


Fig. 3: Number density of voids larger than r , $n_v(r)_c$, obtained for voids found in the distribution of SDSS (red points) and Uchuu-SDSS galaxies (blue points) with $M_r < -20.5$ and $0.02 < z < 0.132$ and predicted by the theoretical framework described in Section 4 with Planck 2015 parameters (black continuous line). Shaded blue region delimits the standard deviation (1σ) of the 32 Uchuu-SDSS lightcones.

Finally, in Figure 4 we can see the VPF, (i.e. the probability that a randomly placed sphere with radius r is empty of objects – galaxies or dark matter haloes) obtained for SDSS and Uchuu-SDSS galaxies. This function is challenging to calculate as we have to take into account the completeness of the survey when randomly placing spheres. The procedure we have followed is similar to the one followed to find real voids: first, we randomly place spheres in the angular plane and in the line-of-sight direction, then we generate points uniformly distributed within the volume of these random spheres and check if the mean completeness of all these points is above 0.9. If it is, we keep the sphere, otherwise, we generate a new one. In other words, our random spheres have to fulfill the same criteria as voids. Next, we calculate the VPF with these survivor spheres, i.e. we divide the total number of these spheres containing no galaxies in their interior by the total number of the survivor spheres.

The results of the VPF obtained for SDSS and Uchuu-SDSS can be seen in Figure 4 and Table 3. Again, we can see that the values obtained for SDSS are compatible, within 1σ , with Uchuu-SDSS values, although the errors for large r are very large. This is again due to the small volume of the samples used.

4. Void statistics theoretical framework

The main void statistics we will study in this work are the number density of voids larger than r , $\bar{n}_v(r)^{\dagger\dagger}$, and the Void Probability Function, $P_0(r)$ (White 1979). For $\bar{n}_v(r)$ we will use the (recalibrated) expression from Betancort-Rijo et al. (2009):

$$\bar{n}_v(r) = \frac{\mu \mathcal{K}(r)}{V} e^{-\alpha \mathcal{K}(r)} \quad (2)$$

^{††}Notice that we use a bar above $n_v(r)$ to quantities predicted by theoretical framework, and without bar to quantities obtained directly by simulations. Additionally, quantities in lowercase letters are in units of volume.

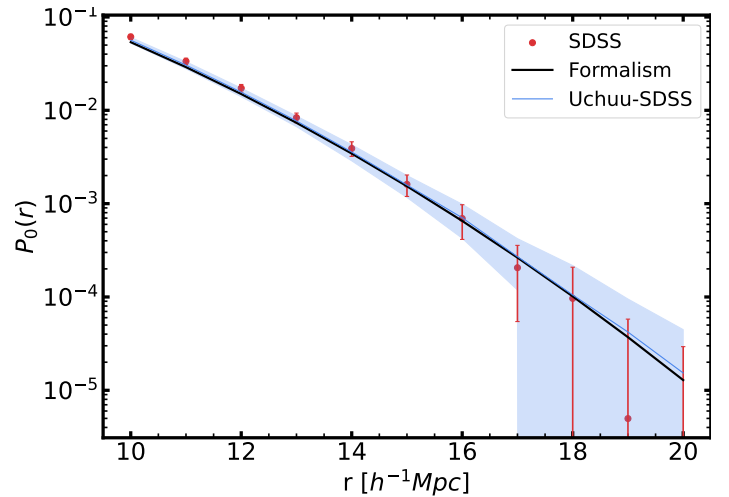


Fig. 4: VPF predicted by theoretical framework described in Section 4 with Planck 2015 parameters (black solid line), and obtained for SDSS (red points) and Uchuu-SDSS (blue solid line) galaxies with $M_r < -20.5$ and $0.02 < z < 0.132$. The shaded blue region and red error bars are the standard deviation of the VPF for the Uchuu-SDSS 32 lightcones.

r	SDSS	Uchuu-SDSS
10	6.127 ± 0.389	5.640 ± 0.073
11	3.354 ± 0.258	3.049 ± 0.047
12	1.728 ± 0.162	1.567 ± 0.032
13	0.835 ± 0.101	0.767 ± 0.204
14	0.390 ± 0.069	0.356 ± 0.014
15	0.161 ± 0.045	0.160 ± 0.008
16	0.0631 ± 0.0242	0.0694 ± 0.0043
17	0.0216 ± 0.0028	0.0270 ± 0.0035
18	$(8.860 \pm 2.018) \times 10^{-3}$	0.0107 ± 0.0025
19	$(3.880 \pm 9.232) \times 10^{-4}$	$(4.16 \pm 1.18) \times 10^{-3}$
20	0.0000 ± 0.0005	$(1.556 \pm 0.699) \times 10^{-3}$

Table 3: VPF obtained for voids found in the distribution of SDSS (first row) and Uchuu-SDSS (second row) galaxies with $M_r < -20.5$ and $0.02 < z < 0.132$. All values are in units of 10^{-2} .

where $\mu=0.588$, $\alpha=1.671$, and

$$\mathcal{K}(r) = \left[-\frac{1}{3} \frac{d \ln P_0(r)}{d \ln r} \right]^3 P_0(r) \quad (3)$$

and

$$V = \frac{4}{3} \pi r^3 \quad (4)$$

In expression 2 it is assumed that $\bar{n}_v(r)$ is an universal functional of $P_0(r)$, so that, independently of the clustering process underlying $P_0(r)$, $\bar{n}_v(r)$ is related to it by an unique expression. However, it has been shown that for white noise it $\mu = 0.68$. So it is clear that this coefficient has a dependence on the clustering properties of the objects considered. But we have found that for the simulations that we have used the quoted values of μ and α are valid. Therefore we shall use these values in all our considerations.

It is important to remark that equation (2) is only valid for $\mathcal{K}(r) \leq 0.46$. For $\mathcal{K}(r) > 0.46$, $\bar{n}_v(r) = 0.313/V$. This quantity, $\mathcal{K}(r)$, measures the rareness of the voids.

Furthermore, equation (2) is only valid for $\sigma_8 > 0.5$, as it has been calibrated to correctly predict the number density of voids for $\sigma_8 \sim 0.9$, as well as for r large enough (i.e. large enough voids, such as $r > 10h^{-1}\text{Mpc}$).

It can be seen that equation (2) differs from the expression of $\bar{n}_v(r)$ given in Betancort-Rijo et al. (2009) (i.e., they give different values of μ , α and write an additional term in the exponential, β). Instead of writing the same values for μ , α and β as in Betancort-Rijo et al. (2009), we have let them be variables and calibrated them with the Uchuu simulation, which has a much larger volume than the simulation used in that work. Therefore, the coefficients given in this work are more accurate.

From equations (2) and (3) we can see that if we know the VPF, we automatically know $\bar{n}_v(r)$, so we first study the VPF and then calculate $\bar{n}_v(r)$ using equation (2).

We can define $P_0(r)$ from a more general statistic that is $P_n(r)$: the probability that a sphere of radius r , placed at random within the distribution, contains n objects. If we assume a Poisson process, we can then write $P_n(r)$ as (Layzer 1954):

$$P_n(r) = \int_0^\infty P(u) \frac{u^n}{n!} e^{-u} du \quad (5)$$

where $P(u)$ is the probability distribution for the integral of the probability density, u , within a randomly placed sphere.

For the root mean square (rms) of the error of the estimation of the VPF we use the following expression:

$$rms(P_0(r))^2 = \frac{9.2 [1 - \omega \bar{n}_v(r)] P_0(r)^2}{N(r)} + \frac{P_0(r)}{N_{spheres}} \quad (6)$$

where $N_{spheres}$ is the number of random spheres used in order to estimate $P_0(r)$ for simulations, $N(r)$ is the number of voids larger than r . This equation is a modification of the expression given in Betancort-Rijo (1992) and Patiri et al. (2006b). We have added a second term, $P_0(r)/N_{spheres}$ to take into account the error due to the finite number of trial random spheres used to calculate the VPF. The first term of equation (6) takes into account the finite volume of the sample.

Finally ω in equation (6) is given by

$$\omega = \frac{32\pi}{3} \bar{R}^3 \left[1 + 2.73 \bar{n}_v(r) \frac{32\pi}{3} \bar{R}^3 \times \left(1 - \frac{3}{4} \frac{\bar{n}_v(r)^{-1/3}}{2\bar{R}} + \frac{1}{8} \left(\frac{\bar{n}_v(r)^{1/3}}{2\bar{R}} \right)^2 \right) \right]^{-1} \quad (7)$$

where \bar{R} is the mean radius of all voids larger than the minimum voids considered.

An explicit computation of each term in $P_n(r)$ can be consulted in Appendix A. There, it can be seen that $P_n(r)$ depends on σ_8 (equation (A.17)), $\Gamma = \Omega_c h$ (equations (A.11), (A.19) and (A.20)) and Ω_m (equations (A.14) and (A.22)). However, the dependence on Ω_m is small, as we will show in Section 5.

Additionally, it can be checked that $P_n(r)$ (in concrete, u), depends on m , which is the mass such that the number density of distinct or central haloes with mass larger than m is equal to the number density of the sample, \bar{n}_{sample} , $\bar{n}(> m) = \bar{n}_{sample}$ (i.e. the mass such that the cumulative halo mass function equals the number density of the sample). If the simulation boxes consisted only on distinct haloes, the mass to be put in m would be simply the mass obtained this way. However, our simulation boxes contain subhaloes, too, and we even have a galaxy simulation

box, galaxy lightcones and, more importantly, a redshift survey of galaxies, so the mass to be put in the theoretical equations is not that trivial.

If our simulation boxes consist on distinct haloes and subhaloes (or galaxies), then the mass to be used in the theoretical equations would be m_g , i.e., the mass such that the cumulative total halo mass function (taking into account distinct haloes and subhaloes) equals the number density of the sample. This mass m_g can be approximately related to m through the following equation:

$$m_g = 1.058^{\sigma(m)} m \quad (8)$$

where $\sigma(m)$ is the rms linear density fluctuation on scale m . It can be shown that, in the interval of masses and cosmological parameters considered in this work, $\sigma(m)$ depends on m , Γ and σ_8 the following way:

$$\sigma(m) = 2.035 \left(\frac{m}{4.039} \right)^{-\frac{0.475}{3}} \left(\frac{\Gamma}{0.1754} \right)^{0.27} \left(\frac{\sigma_8}{0.8159} \right) \quad (9)$$

Additionally, an expression for m_g depending on the \bar{n}_{sample} , σ_8 and Γ can be found:

$$m_g = 1.0463 \times 4.039 \left(\frac{\sigma_8}{0.8159} \right)^{0.402} \left(\frac{\Gamma}{0.1754} \right)^{0.109} \left(\frac{F(\bar{n}_{sample})}{4.047} \right) \quad (10)$$

where

$$F(\bar{n}) = -\frac{1.267 \times 10^{-8}}{\bar{n}^2} + \frac{1.289 \times 10^{-2}}{\bar{n}} - 0.248 \quad (11)$$

This last function, $F(\bar{n})$ defines the dependence of the mass m with the number density of the sample, \bar{n} . It is important to remark that \bar{n}_{sample} is the number density of galaxies corrected from completeness in the case we use redshift surveys or lightcones.

Equation (10) is a good approximation to m_g (i.e. the value of m to be used in the theoretical framework, equations A.9-A.12) as a function of cosmological parameters and \bar{n}_{sample} , while the abundance matching provides its exact value. However, the dependence on σ_8 and Γ is quite small and it is swamped by small error in expressions A.9-A.12 (which have been fitted to the results of a complex procedure) that have a much stronger dependence on σ_8 and Γ . So we have found that the best agreement between the theoretical framework and the simulations are obtained holding m_g fixed for given values of \bar{n}_{sample} .

The value of m_g has been chosen taking into account the value predicted for Uchuu, but decreasing its value a little bit so the χ^2 value for the three small boxes, defined using the VPF, is between the range

$$\chi^2 = \nu \pm \sqrt{2\nu} \quad (12)$$

where ν is the number of degrees of freedom. In order to calculate the chi square function, we have used the VPF predicted by the theoretical framework developed in this work, and the VPF obtained directly for each simulation box. We have used the radius bins with $r \geq 14h^{-1}\text{Mpc}$, $r \leq 21h^{-1}\text{Mpc}$ and $\Delta r = r_{i+1} - r_i = 1h^{-1}\text{Mpc}$ (i.e., 8 bins, so $\nu = 8$). Therefore, χ^2 must be between

$\chi^2 > 3.3$ and $\chi^2 < 12$. We can see that if we choose $m_g = 4.66$, the value of χ^2 for Uchuu, P18, LowS8 and VeryLows8 are, respectively, 11.20, 6.37, 11.86 and 11.74. If we increase the value of m_g to 4.67, then $\chi^2 > 12$ for LowS8 and VeryLowS8 boxes, and if we decrease the value of m_g to 4.65, then $\chi^2 = 11.89$ for Uchuu, which is our high resolution simulation. Therefore, $\chi^2 = 4.66$ is the safer choice.

We can see that so far our theoretical framework depends on 4 cosmological parameters: σ_8 , Ω_c , H_0 and Ω_m (it doesn't depend on Ω_Λ as we impose a flat Λ CDM model, and the dependence of the formalism with Ω_c and H_0 is only through $\Gamma = \Omega_c h$). However, we can decrease the number of free parameters by relating Ω_m and $\Omega_b = \Omega_m - \Omega_c$, where Ω_b is the baryonic matter density parameter. From Planck 2018 (Planck Collaboration et al. 2016) we get $\alpha \equiv \Omega_b/\Omega_m = 0.157$. Therefore, $\Omega_c = (1 - \alpha)\Omega_m$ and $\Omega_b = \alpha\Omega_m$, and our final parameters are σ_8 , Ω_m and H_0 .

Before using the theoretical framework to constrain σ_8 and Ω_m and H_0 in the SDSS survey, it is important to check if the theoretical equations are accurate and have enough precision to recover the real values of σ_8 , Ω_m and H_0 from simulations with different values of the parameters. In order to do this, we use the halo simulation boxes that we have presented in Section 2.2, which have different values of σ_8 .

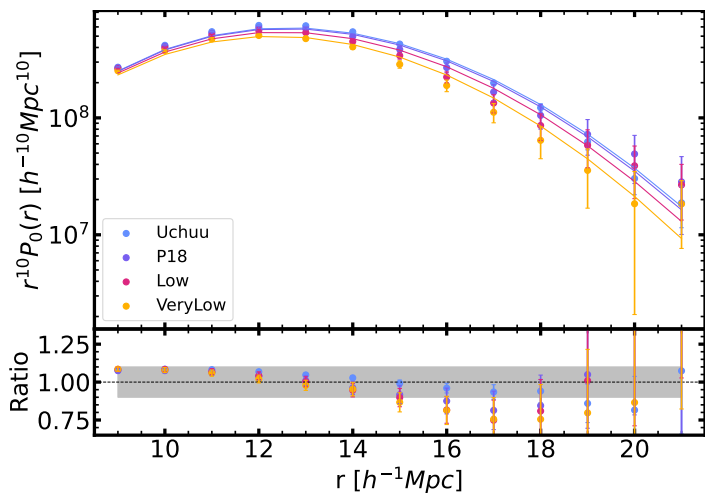


Fig. 5: In top panel the VPF in real space is shown for the theoretical framework (lines) and simulations (dots), while the ratio between simulations and theoretical framework is shown in bottom panels for the Uchuu, P18, Low and VeryLow box catalogs with number density $\bar{n} = 3 \times 10^{-3} h^{-3} \text{Mpc}^3$. Shaded region in bottom panel indicates delimits the region between 0.9 and 1.10 for the ratio.

In the upper panel of Figure 5 the VPF values (multiplied by r^{10} to differentiate more easily the values of each simulation for large radii) predicted by the theoretical framework (continuous lines) and obtained by simulations (points) for the four halo simulation boxes in real space are shown. The numerical values are presented in Table B.1 in Appendix B. It can be seen that the dependence of the VPF predicted by the theoretical framework is the same as that shown by simulations, that is, the lower σ_8 is, the lower $P_0(r)$ is for each radius bin. In the bottom panel of the same Figure, the ratio between simulations and theoretical framework is shown. It can be checked that all values are within (or compatible with) 10% of the ratio.

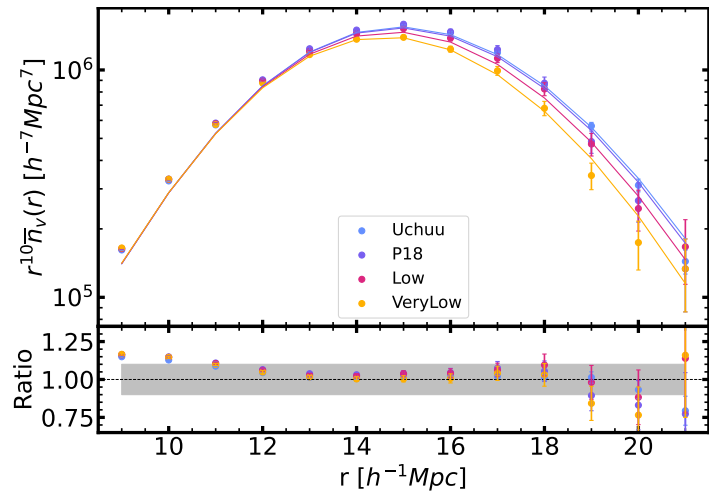


Fig. 6: In top panel the number density of voids larger than r in real space is shown for the theoretical framework (lines) and simulations (dots), while the ratio between simulations and theoretical framework is shown in bottom panels for the Uchuu, P18, Low and VeryLow box catalogs with number density $\bar{n} = 3 \times 10^{-3} h^{-3} \text{Mpc}^3$. Shaded region in bottom panel indicates delimits the region between 0.9 and 1.10 for the ratio.

In the upper panel of Figure 6 the values of the number density of voids larger than r predicted by the theoretical framework (continuous lines) and obtained by simulations (points) for the 4 halo simulation boxes in real space can be seen. In the bottom panel of the same Figure, the ratio between simulations and theoretical framework is shown. Again, the agreement between the theoretical framework and the simulation values is good, especially for r between 12 and 18 $h^{-1} \text{Mpc}$.

It is important to note that the values of the VPF and $n_v(r)$ for the three small box catalogs (each with a different value of σ_8) are very similar for small values of r ($r < 13 h^{-1} \text{Mpc}$). The differences between the three simulations begin to become important for $r > 16 h^{-1} \text{Mpc}$, approximately. This is why these are the only voids we consider in order to constrain σ_8 in the next section.

The next step is to repeat this process in redshift space and compare with simulations in order to check if the theoretical framework still works in this space. This is done in Appendix B.2. In concrete, in Figures B.2 and B.3 the VPF and number density of voids larger than r in redshift space are shown for the four halo simulation boxes. The agreement is still good, so we can conclude that the theoretical framework works in redshift space, too.

Now, we can discuss the results obtained for SDSS survey and Uchuu-SDSS lightcones. In Figure 3 we have already shown the abundance of voids larger than r for SDSS and Uchuu-SDSS. The values given by the theoretical framework are shown in the same figure with a continuous black line. We can see that the agreement between the theoretical framework and Uchuu-SDSS is good for $r > 14 h^{-1} \text{Mpc}$.

Additionally, in Figure 4 we have already shown the VPF for SDSS and Uchuu-SDSS. The values given by the theoretical framework are shown in this Figure, too, with a continuous black line. We can see that the agreement between the theoretical framework and Uchuu-SDSS is quite good, and is compatible within 1σ with SDSS values.

To sum up, we have checked in this section that the theoretical framework successfully predicts the void statistics studied

in this work for the four halo simulation boxes and for Uchuu-SDSS lightcones, and it is compatible with SDSS survey statistics within 1σ . Therefore, we are ready to constrain σ_8 and Ω_m and H_0 from the SDSS galaxy sample we have chosen.

5. Bayesian analysis for cosmological parameters inference

In order to infer σ_8 , Ω_m and H_0 from the number density of voids larger than r , we use a Bayesian analysis and Markov chain Monte Carlo (MCMC) technique in order to sample the posterior distribution of the considered parameter sets, Θ :

$$\mathcal{P}(\Theta|\mathcal{D}) \propto \mathcal{L}(\mathcal{D}|\Theta)p(\Theta) \quad (13)$$

where $p(\Theta)$ is the prior distribution, and $\mathcal{L}(\mathcal{D} | \Theta)$ is the likelihood, calculated as

$$\mathcal{L}(\mathcal{D}|\Theta) = \prod_{i=1}^6 \frac{1}{\sigma_i} \exp\left(-\frac{(N_{v,i}(\mathcal{D}) - \bar{N}_{v,i}(\Theta))^2}{2\sigma_i^2}\right) \quad (14)$$

where $N_{v,i}(\mathcal{D})$ is the number of voids within i th bin from simulations or data, $\bar{N}_{v,i}(\Theta)$ is calculated from equation (2) subtracting the value in the $(i+1)$ th bin (or $r + \Delta r$), and σ_i is the rms of $N(r_i)$:

$$\sigma_i = rms(\bar{N}_{v,i}(\Theta)) = \sqrt{\bar{N}_{v,i}(\Theta)/N_r} \quad (15)$$

where N_r represents the number of realizations for each simulation. For the simulation boxes and SDSS, N_r is equal to 1, indicating a single realization for each set of cosmological parameters and one SDSS survey. However, in the case of Uchuu-SDSS, N_r is 32, as we have 32 lightcones of this particular type.

In this work, we use voids larger than $r = 16h^{-1}\text{Mpc}$ to constrain the cosmological parameters of interest, so in equation (14) we consider the radius bins starting from $r = 16h^{-1}\text{Mpc}$ to $r = 21h^{-1}\text{Mpc}$ (i.e. 6 bins with width $\Delta r = 1h^{-1}\text{Mpc}$).

With equation (13) the best estimate of the parameters Θ may be obtained by maximising $\mathcal{P}(\Theta|\mathcal{D})$ with respect to the parameters Θ . In order to do this, we assign to all the parameters (σ_8 , Ω_m and H_0) wide enough priors (see first column of Table 4).

	Voids-Only	Voids+KiDS	Voids+DES
σ_8	[0.5-1.4]	[0.5-2.2]	[0.5-2.5]
Ω_m	[0.15-0.5]	[0.15-0.686]	[0.15-0.9]
H_0	[40-140]	[64-82]	[55-91]

Table 4: Range of each parameter used in order to constrain these parameters considering only the void statistics developed in this work (first column), and in order to compare our confidence level contours with KiDS-1000, KiDS-1000+DESY3 (second column) and DESY3 (third column) in Figure 11.

Additionally, we may want to combine our results with other works. To do this, we multiply our likelihood by the likelihood of the work we want to combine our results with. In this work, we combine our results with Planck 2018 (Aghanim et al. 2020) and some Weak Lensing works, such as KiDS-1000 and DESY3 (Dark Energy Survey and Kilo-Degree Survey Collaboration et al. 2023). We use Cobaya (Torrado & Lewis 2019; Torrado & Lewis 2021) in order to run MCMC sampler for SDSS

voids, so Planck's likelihood can easily be combined with SDSS voids likelihood. However, the likelihoods of the weak lensing works used in this study are not incorporated in Cobaya, and CosmoSIS (Zuntz et al. 2015) must be used instead. However, CosmoSIS is very slow for our purpose, so we have used a brand new code called CombineHarvesterFlow* which allows one to efficiently sample the joint posterior of two non-covariant experiments with a large set of nuisance parameters (Taylor et al. 2024). In concrete, CombineHarvesterFlow trains normalizing flows on posterior samples to learn the marginal density of the shared parameters. Then by weighting one chain by the density of the second flow, one can find joint constraints.

The confidence level contours in the plane σ_8 - H_0 (fixing Ω_m in each case to its real value, see Table 1) obtained for the four halo simulation boxes can be seen in the Appendix B. There, we can check that we recover the values of σ_8 and H_0 of the simulations within 1σ (2σ) in real (redshift) space. Therefore, we can infer these cosmological parameters in Uchuu-SDSS lightcones.

6. Assessing the potential of voids statistics to constrain cosmological parameters (using Uchuu-SDSS)

Before constraining any cosmological parameter, we will see how does the theoretical framework behave when we fix one of the three cosmological parameters on which the theoretical framework depends on and we let the other two parameters vary in a large range. We will do this for Uchuu-SDSS lightcones in order to check if the theoretical framework is able to recover successfully the cosmological parameters of Planck 2015 (Planck Collaboration et al. 2016), which are the real values of Uchuu-SDSS cosmological parameters.

In order to do this, we will plot the confidence level contours obtained as explained above in each of the three possible planes ($\sigma_8 - \Omega_m$, σ_8 - H_0 and Ω_m - H_0) fixing the remaining parameter to three different constant values to check if the formalism is sensitive to this parameter.

Figure 7 shows the contours of 68% and 95% confidence level in the planes $\sigma_8 - \Omega_m$ (first row), σ_8 - H_0 (second row) and Ω_m - H_0 (third row) planes. For each plane, the value of the remaining parameter (H_0 , Ω_m and σ_8 for first, second and third row, respectively) has been fixed at different values which are indicated in the boxes inside each subplot. It can be seen that Planck 2015 values are inside the 68% confidence level region only when the remaining parameter is fixed to a value close to Planck 2015 parameter. For example, if we focus on $\sigma_8 - \Omega_m$ contour, we can see that the Planck values of σ_8 and Ω_m are not compatible with Uchuu-SDSS statistics predicted by our theoretical framework if $H_0 = 0.6$ or $H_0 = 0.8$, but it is compatible with these statistics if $H_0 = 0.7$, which is the closest value to the one of Planck 2015 (see Table 1). The same effect can be seen in the rest of the planes.

As we mentioned in Section 4, the theoretical framework mainly depends on σ_8 and $\Gamma = \Omega_c h$, although it also depends on Ω_m , but this dependence is small. We can see this in the last row of Figure 7, where the contours obtained for $\sigma_8 - \Gamma$ plane are shown for different values of Ω_m which are indicated inside the box of each figure. It can be seen that the contours slightly displaces with different values of Ω_m , but this displacement is not as noticeable as it is in $\sigma_8 - \Omega_m$ and σ_8 - H_0 planes. Therefore, we can conclude that the theoretical framework depends mainly on σ_8 and $\Gamma = \Omega_c h$ parameters.

*<https://github.com/plttaylor16/CombineHarvesterFlow>

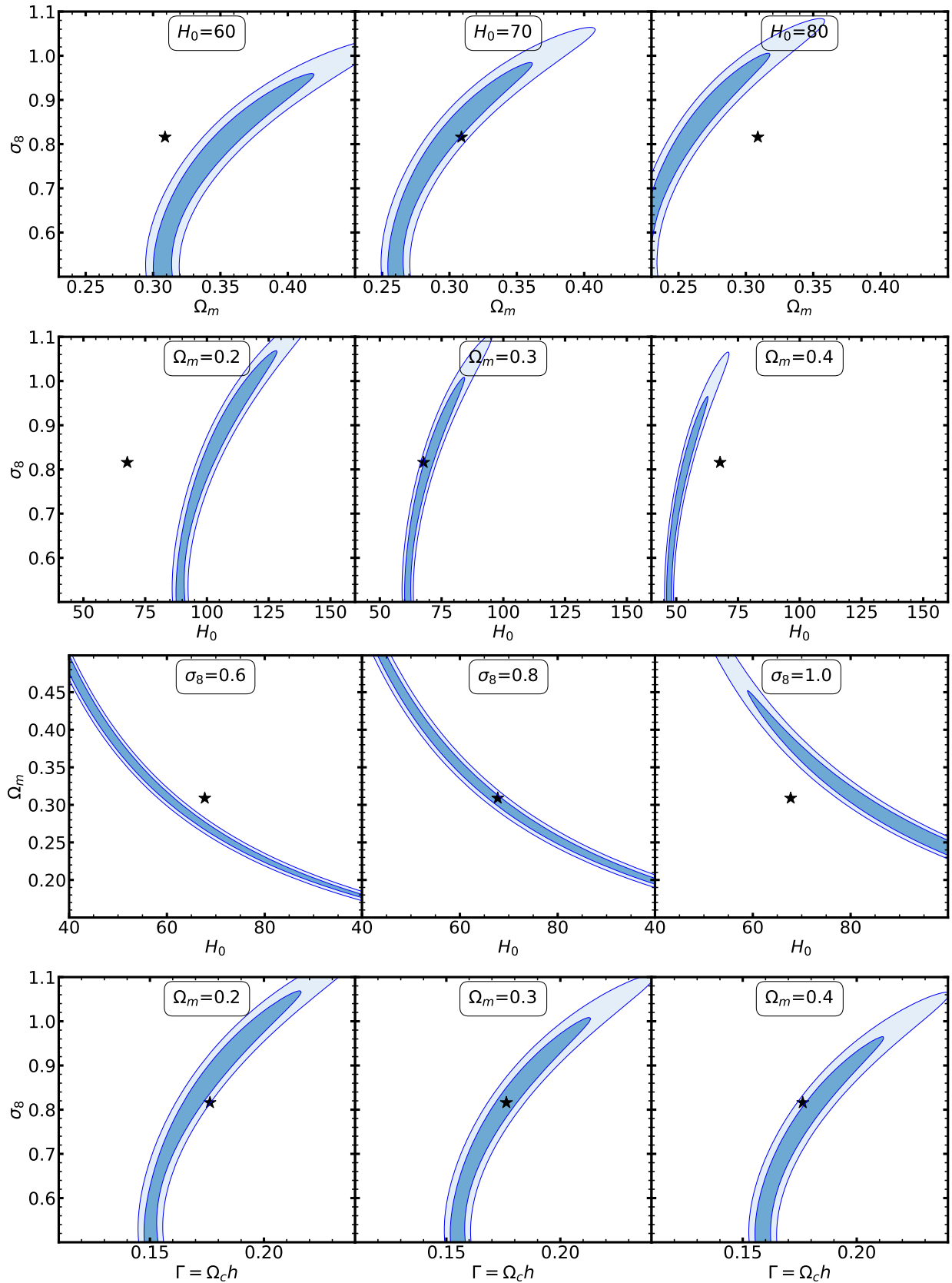


Fig. 7: Confidence level contours in Ω_m - H_0 (first row), σ_8 - H_0 (second row), σ_8 - Ω_m (third row) and σ_8 - Γ (fourth row) planes obtained for Uchuu-SDSS lightcones using the Maximum Likelihood test with Bayesian approach with the theoretical framework developed in this work. For each plane, the value of the remaining parameter has been fixed to the value indicated in the box inside each subplot. The contours indicate the 68% (1σ) and 95% (2σ) confidence levels. The black star is the value from Planck 2015 (Planck Collaboration et al. 2016). The last row panels show a small dependence on Ω_m .

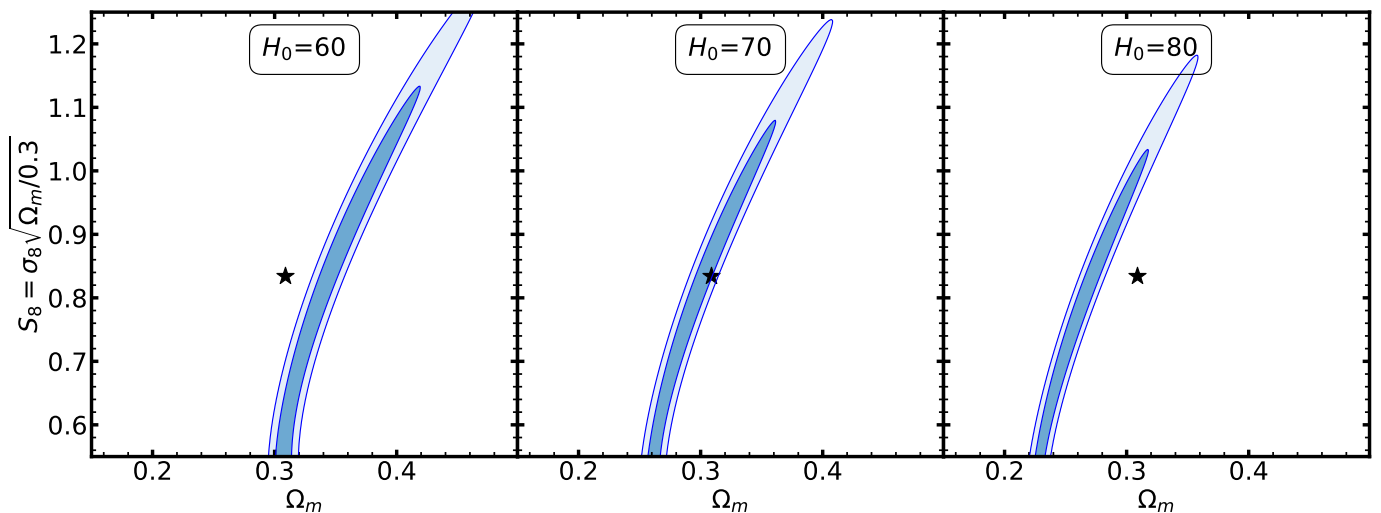


Fig. 8: Confidence level contours in $S_8 - \Omega_m$ plane obtained for Uchuu-SDSS lightcones using the Maximum Likelihood test with Bayesian approach with the theoretical framework developed in this work. The value of H_0 has been fixed at a value which is indicated in the box inside each subplot. The contours indicate the 68% (1σ) and 95% (2σ) confidence levels. The black star is the value from Planck 2015 (Planck Collaboration et al. 2016).

The last important contour to study is the one obtained in $S_8 - \Omega_m$ plane. This contour is shown in Figure 8 for different values of H_0 . It can be seen that $H_0 = 70$ (which is the closest value to the real one of Uchuu simulations) is compatible with Uchuu-SDSS within 1σ , but $H_0 = 60$ and $H_0 = 80$ are not.

The last step we can take in order to assess the potential of the theoretical framework to constrain cosmological parameters is inferring σ_8 , Ω_m and H_0 values. In order to do this, we use Cobaya and the priors indicated in the first column of Table 4. The inferred values of these cosmological parameters provided by Cobaya are: $\sigma_8 = 0.782^{+0.166}_{-0.183}$, $\Omega_m = 0.302^{+0.106}_{-0.099}$, $H_0 = 75.42^{+25.94}_{-23.29}$, $\Gamma = 0.1769^{+0.0228}_{-0.0208}$ and $S_8 = 0.776^{+0.205}_{-0.208}$. Our uncertainties are very wide (in comparison of Planck’s uncertainties), specially the uncertainty of H_0 . With these wide uncertainties, we can check that our constrained values are compatible with Planck values within 1σ .

The confidence level contours for Uchuu-SDSS can be seen in the right part of Figure 9. We can see that the 68% confidence level contour closes for high values of σ_8 , although it doesn’t for low values as we haven’t explored regions with $\sigma_8 < 0.5$ because, as mentioned before, many of the equations of the formalism are not valid for $\sigma_8 < 0.5$.

7. Cosmological Constraints from SDSS survey

In this part of the work, we show the constraints obtained for SDSS redshift survey. Firstly, we show the constraints we obtain directly from the theoretical framework developed in this work. Next, we combine our results with Planck 2018 and, finally, we do it with Weak Lensing works such as KiDS-1000, DESY3 and the combination of both works, KiDS-1000+DESY3.

7.1. SDSS voids-only constraints

The initial contour we examine lies within the plane showcasing the core parameters of our theoretical framework: the $\sigma_8 - \Gamma$ plane, as depicted in Figure 10. In this illustration, we have also included the confidence level contours for Uchuu-SDSS and Planck 2018. We can see that Planck’s contour is completely in-

side Uchuu-SDSS and SDSS voids contours, so we don’t expect to get a big improvement in the constrained values of the parameters when combining. Therefore, in order not to waste computational resources, we have not made such a combination.

From Figure 10 it can be seen that the confidence level region for Planck 2018 is entirely encapsulated within the SDSS contour at the region of 2σ , indicating that the constraints from both samples are statistically compatible in this limit.

In the left part of Figure 9 we can observe the confidence level contours obtained in the rest of the planes: $\Omega_m - H_0$, $\sigma_8 - H_0$ and $\sigma_8 - \Omega_m$.

In the first column of Table 5 we can observe the constrained values directly obtained from our theoretical framework of σ_8 , Ω_m , H_0 , Γ and S_8 for SDSS survey. From this Table, it can be seen that the uncertainties of σ_8 and Γ are much larger for SDSS than for Uchuu-SDSS because of the huge difference in the volumes between them. However, this is not the case for Ω_m and H_0 . This is because σ_8 and Γ are the fundamental parameters of the theoretical framework (and S_8 depends strongly on σ_8). With these large errors, our constraints from SDSS are compatible with Planck’s within 1σ .

As we have already mentioned, we are not going to combine our results with Planck 2018, however we can show the behaviour of the theoretical framework for SDSS when two of the three cosmological parameters adopt a value close enough (or a range centered in the best-fit value of Planck 2018 and with an amplitude of 3σ , for example) to Planck values. These constraints can be seen in the second column of Table 5. We can see that the uncertainties decrease considerably for all parameters but S_8 . However, any parameter obtained this way is compatible within 1σ with Planck 2018. Nevertheless, it is important to remark the low mean values we get for Ω_m and H_0 the formalism predicts even if we restrict to an interval of 3σ ’s of Planck for the other two parameters.

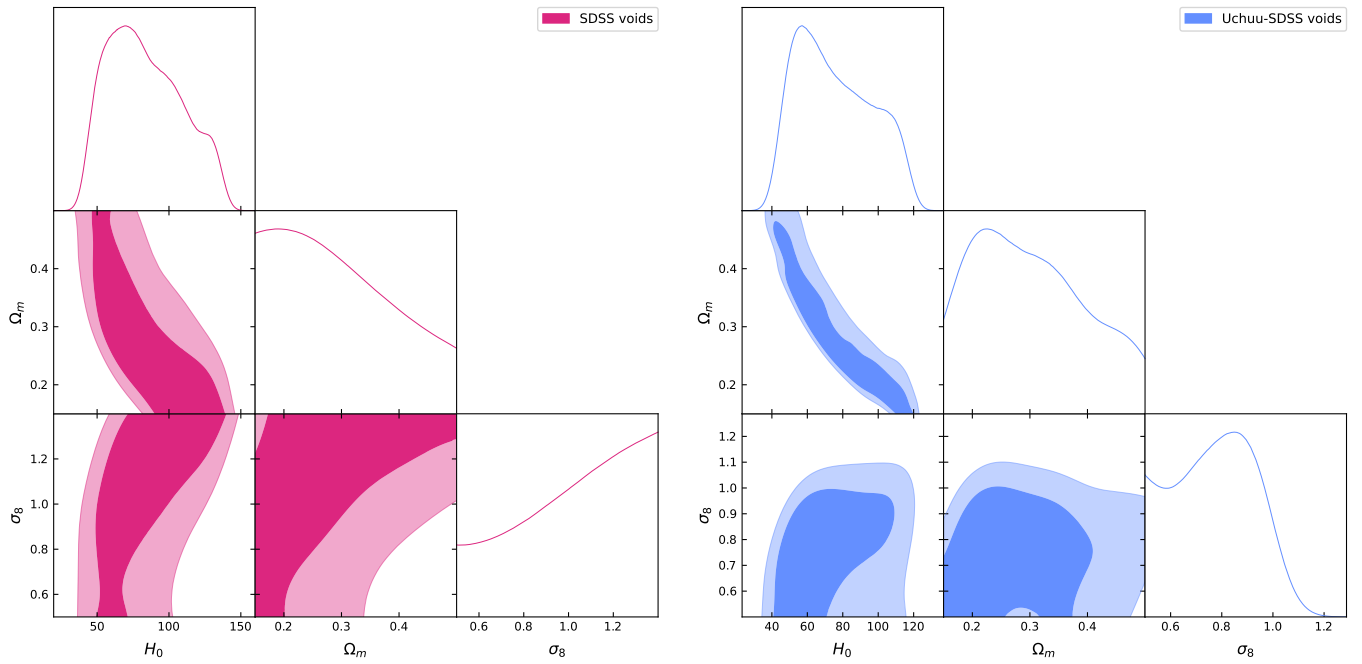


Fig. 9: Confidence level contours in Ω_m - H_0 , σ_8 - H_0 and $\sigma_8 - \Omega_m$ planes obtained for SDSS redshift survey (left) and Uchuu-SDSS lightcones (right) using the Maximum Likelihood test with Bayesian approach with the theoretical framework developed in this work. The contours indicate the 68% (1σ) and 95% (2σ) confidence levels.

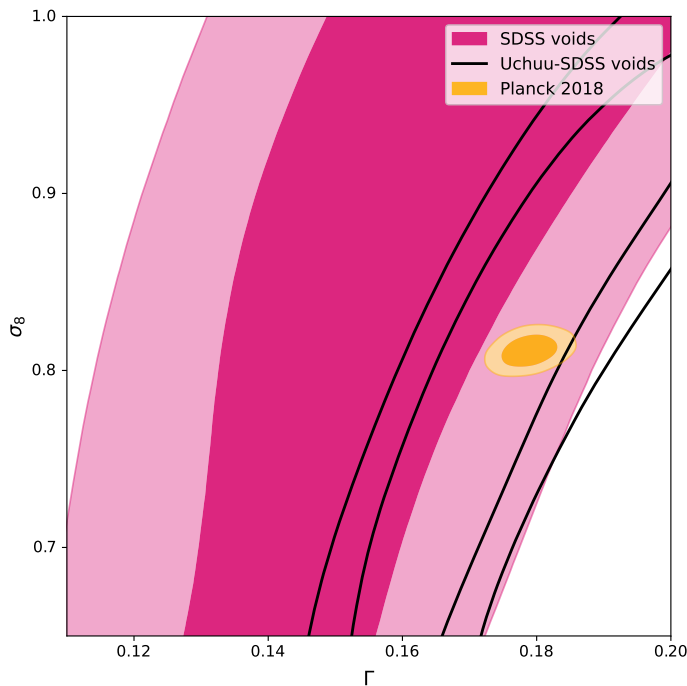


Fig. 10: Confidence level contours in $\sigma_8 - \Gamma$ plane obtained for Uchuu-SDSS voids and SDSS voids using the Maximum Likelihood test with Bayesian approach with the theoretical framework developed in this work. We also show the confidence level contour for Planck 2018. The contours indicate the 68% (1σ) and 95% (2σ) confidence levels.

	SDSS voids	SDSS voids (3σ -P)	Planck
σ_8	$1.028^{+0.273}_{-0.305}$	$1.003^{+0.118}_{-0.125}$	0.8111 ± 0.0060
Ω_m	$0.296^{+0.110}_{-0.102}$	$0.265^{+0.033}_{-0.033}$	0.3153 ± 0.0073
H_0	$83.43^{+29.27}_{-27.70}$	$58.86^{+7.34}_{-6.95}$	67.36 ± 0.54
Γ	$0.1947^{+0.0578}_{-0.0516}$	$0.1524^{+0.017}_{-0.016}$	0.1772 ± 0.0027
S_8	$1.017^{+0.363}_{-0.359}$	$1.061^{+0.406}_{-0.415}$	0.832 ± 0.013

Table 5: Constraints of σ_8 , Ω_m , H_0 (in units of $\text{kms}^{-1}\text{Mpc}^{-1}$), $S_8 = \sigma_8 \sqrt{\Omega_m/0.3}$ and $\Gamma = \Omega_c h$ for SDSS voids (first column), SDSS voids considering uniform priors centered in Planck 2018 best-fit values and with an amplitude of 3σ the 68% given by Planck 2018 (second column) and Planck 2018 best-fit values (Aghanim et al. 2020) (third column), with errors calculated as the 68% uncertainties.

7.2. SDSS voids + Weak Lensing

Finally, we can combine our results with KiDS-1000 and DESY3. These results are presented in [Dark Energy Survey and Kilo-Degree Survey Collaboration et al. \(2023\)](#).

When combining our results with other studies, such as those mentioned above, caution must be taken, as the same range for all the parameters must be considered if we want to visually compare the confidence level contours obtained in each case and combine the chains using `CombineHarvesterFlow`. This allow us to make a fair comparison of our confidence level contours with those of Weak Lensing. However, as we have seen previously, the theoretical framework used in this work depends on the parameters σ_8 , Ω_m , and H_0 . In Weak Lensing studies, A_s (DESY3) or S_8 (KiDS and KiDS-1000+DESY3) are sampled instead of σ_8 , and ω_c and ω_b in-

	SDSS voids	KiDS-1000	DESY3	SDSS+KiDS	SDSS+DESY3	SDSS+KiDS+DESY3	Planck
σ_8	$1.028^{+0.273}_{-0.305}$	$0.833^{+0.133}_{-0.146}$	$0.816^{+0.076}_{-0.065}$	$0.859^{+0.050}_{-0.051}$	$0.881^{+0.049}_{-0.047}$	$0.858^{+0.040}_{-0.040}$	0.8111 ± 0.0060
Ω_m	$0.296^{+0.110}_{-0.102}$	$0.270^{+0.056}_{-0.102}$	$0.297^{+0.040}_{-0.060}$	$0.247^{+0.027}_{-0.026}$	$0.256^{+0.024}_{-0.023}$	$0.257^{+0.023}_{-0.020}$	0.3153 ± 0.0073
H_0	$83.43^{+29.27}_{-27.70}$	$75.42^{+1.70}_{-2.13}$	73.83 ± 4.98	$74.20^{+5.05}_{-5.18}$	$74.72^{+5.36}_{-5.56}$	$74.17^{+4.66}_{-4.66}$	67.36 ± 0.54
S_8	$1.017^{+0.363}_{-0.359}$	$0.764^{+0.031}_{-0.023}$	$0.802^{+0.023}_{-0.019}$	$0.775^{+0.020}_{-0.019}$	$0.811^{+0.019}_{-0.017}$	$0.794^{+0.016}_{-0.016}$	0.832 ± 0.013

Table 6: Constraints of σ_8 , Ω_m , H_0 (in units of $\text{kms}^{-1}\text{Mpc}^{-1}$) and $S_8 = \sigma_8 \sqrt{\Omega_m/0.3}$ for SDSS voids (first column), KiDS-1000 (second column), DESY3 (third column) (Dark Energy Survey and Kilo-Degree Survey Collaboration et al. 2023), SDSS voids+KiDS-1000 (fourth column), SDSS+DESY3 (fifth column), SDSS+KiDS-1000+DESY3 (sixth column) and Planck 2018 (Aghanim et al. 2020) (last column), with errors calculated as the 68% uncertainties.

stead of Ω_m (KiDS and KiDS-1000+DESY3). Therefore, what we have done is to determine which priors on σ_8 and Ω_m correspond to the aforementioned priors, ensuring compatibility across these parameters. Nevertheless, it's important to consider a significant limitation: our formalism is not valid for σ_8 values less than 0.5, as mentioned earlier, nor for Ω_m values less than 0.15. Thus, we have added this additional condition in the priors. This may slightly affect the process of combining chains using CombineHarvesterFlow, but, as we will see later, the effect will be very small because of the relative orientation and size of SDSS voids and Weak Lensing confidence level contours.

The ranges we have used for our chains when combining with KiDS-1000 and DESY3 can be seen in the second and third columns, respectively, of Table 4. We can see that the range of H_0 used in these works is very narrow.

The confidence level contour in the plane $\sigma_8 - \Omega_m$ using these ranges can be seen in Figure 11. In this Figure, the confidence level contour for SDSS voids with the same ranges as the different weak lensing works considered are shown, as well as each weak lensing work confidence level contour and the combination of SDSS voids with these three contours. We can see that SDSS voids contour is almost orthogonal to the three Weak Lensing contours (as expected, see Contarini et al. (2023) for more details), so we can anticipate that our constrained values of σ_8 and Ω_m will have smaller uncertainties than the values of the original work.

The best-fit values of σ_8 , Ω_m , H_0 and S_8 obtained from SDSS voids, KiDS-1000 and DESY3 can be seen in the first three columns of the Table 6. The combination of SDSS voids with KiDS-1000, DESY3 and KiDS-1000+DESY3 can be seen in the fourth, fifth and sixth columns, respectively, of the same Table.[†] We can see that the effect of combining these three Weak Lensing works with SDSS voids is increasing the value of σ_8 , as the best-fit value of SDSS voids is very high, which means implies a decrease in the best-fit value of Ω_m (from Figure 11 we can see that the three Weak Lensing works predicts a strong correlation between σ_8 and Ω_m , and that if one increases, the other decreases. This correlation is kept also when combining Weak Lensing works with SDSS voids).

We can also see from table 6 that there is an increase in the uncertainties of H_0 when combining Weak Lensing with SDSS voids, which is caused by our huge uncertainties in this param-

eter. However, the uncertainties of the rest of the parameters are decreased by a factor 2-3, approximately, with respect to the original errors of each Weak Lensing work.

As a final remark, we can see from table 6 that any value of H_0 or Ω_m obtained when combining SDSS voids with the three Weak Lensing works are compatible with Planck 2018 within 1σ (for Ω_m , they are within 2.3σ , approximately). We can also see that S_8 value from SDSS voids + DESY3 is compatible with Planck 2018 within 1σ , but SDSS voids + KiDS-1000 and SDSS voids + KiDS-1000+DESY3 aren't (they are compatible with Planck 2018 considering the uncertainty as 1.8σ and 1.6σ , respectively).

8. Comparison with other works about voids

In this part of the work we compare our constraints in σ_8 , H_0 and $S_8 = \sigma_8 \sqrt{\Omega_m/0.3}$ with those obtained in other works that also use voids statistics to constrain these same parameters.

The first work we can compare our results with is Contarini et al. (2024), where the values of S_8 and H_0 are constrained using the void size function (abundance of voids with radius r) predicted by the excursion set theoretical framework (Press & Schechter 1974; Sheth & Van De Weygaert 2004) by means of an extension of the popular volume-conserving model (Vdn model, Jennings et al. 2013). The constraints they obtain combining the voids counts with the void shapes (Hamaus et al. 2020) are $\sigma_8=0.809^{+0.072}_{-0.068}$, $\Omega_m=0.308^{+0.021}_{-0.018}$, $H_0=67.3^{+10.0}_{-9.1}$ and $S_8=0.813^{+0.093}_{-0.068}$. The redshift survey they use in order to constrain these cosmological parameters is BOSS DR12 (Dawson et al. 2013). In concrete, they use LOWZ and CMASS target selections, and divide the catalogs into two redshift bins: $0.2 < z \leq 0.45$ and $0.45 < z < 0.65$. This sample has a physical volume approximately 60 times larger than the volume of the sample used in this work (according to Reid et al. (2015) the volume of CMASS is 5.1Gpc^3 and the one of LOWZ is 2.3Gpc^3 , which translates into a total volume of $2.3 \times 10^9 h^{-3}\text{Mpc}^3$). If we take into account that errors (using only void statistics, without combining with Weak Lensing or other works) scales as $V^{-1/4}$ with volume (see appendix C), we can calculate how much errors would decrease if we would use a redshift survey like BOSS DR12 with our theoretical framework: $60^{-1/4} \sim 0.36$, i.e. our errors (calculated as 68% uncertainties) would decrease approximately 3 times, so we would have similar constraints with our theoretical framework (without combining with any other work) than with Vdn model+Void Shapes if we used a sample with BOSS DR12 volume.

The other work we can compare our results with is Sahlén et al. (2016). In this work, galaxy cluster and void abundances

[†]It is important to remark that CombineHarvesterFlow gives the inferred parameters obtained from the combination for two chains in two different ways: weighting SDSS voids chains or weighting Weak Lensing chains. The results we have presented correspond to weighting SDSS void chains, but we have checked that weighting Weak Lensing chains we obtain compatible results.

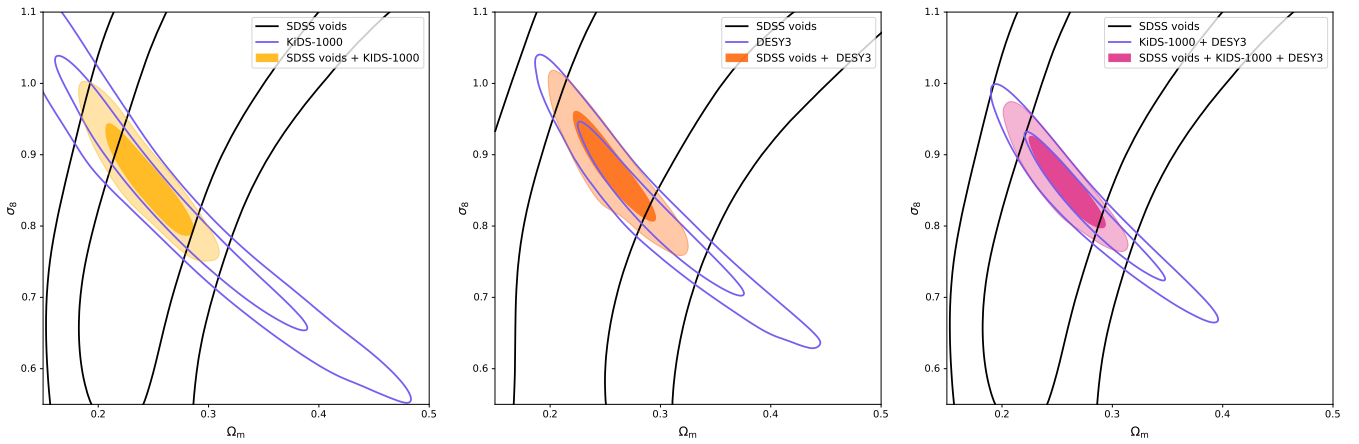


Fig. 11: In the left, middle and right panels we have presented KiDS-1000, DESY3 and KiDS-1000+DESY3 contours, respectively, with SDSS voids contours in the plane $\sigma_8 - \Omega_m$ using the same parameter ranges in order to make a fair comparison, and the combination of SDSS voids with each weak lensing work. In table 4 the parameter ranges of each work are indicated.

are combined using extreme-value statistics on a large cluster and a void aligned with the Cold Spot (CS) in the CMB (CS void) (Finelli et al. 2016). This way they obtain a value of $\sigma_8 = 0.95 \pm 0.21$ for a flat Λ CDM universe. This constraint is also compatible with CMB value as well as Weak Lensing values.

9. Summary

In this work, we have made use of the theoretical framework developed in Betancort-Rijo et al. (2009) and recalibrated the expression for the number density of voids larger than r (see equation (2)) using the Uchuu halo simulation box with a number density of haloes equal to $3 \times 10^{-3} h^{-3} \text{Mpc}^3$, which has a larger volume than the simulation used in the aforementioned work ($V = 2000^3 h^{-3} \text{Mpc}^3$). The most important results obtained in this work are the following:

- we have proved that the number density of voids larger than r and the Void Probability Function (VPF, i.e., the probability that a randomly placed sphere with radius r is empty of galaxies or haloes) of SDSS galaxies with $M_r < -20.5$ (where M_r is the absolute magnitude in r -band), $z_{\min} = 0.02$ and $z_{\max} = 0.132$, and Uchuu-SDSS galaxies with the same characteristics, are compatible within 1σ ,
- we have demonstrated that our theoretical framework predicts successfully the Void Probability Function and the abundance of large voids for the four halo simulation boxes with different values of σ_8 ($\sigma_8 = \{0.8159, 0.8102, 0.75, 0.65\}$) and Uchuu-SDSS lightcones used in this work, again within 1σ ,
- we have used a bayesian analysis for all halo simulation boxes and we have calculated the contours for 68% (1σ) and 95% (2σ) confidence levels in σ_8 - H_0 plane (fixing Ω_m in each case to its real value, see Table 1), and proved that we recover the real values of σ_8 and H_0 of each halo simulation box within 1σ in real space, and 2σ in redshift space,
- supposing that the ratio of Ω_b/Ω_m is constant and given by Planck 2018, we have studied, how much Uchuu-SDSS contours change in each plane mentioned above if we fix the values of the remaining parameter to three sufficiently different values. We have seen that these contours are very sensitive to these changes, so if we considered a survey with the same volume as Uchuu-SDSS we could constrain with high precision each parameter.

- we have also shown that the dependency of the theoretical framework on Ω_m is small and that the main dependence of is through $\Gamma = \Omega_c h$ and σ_8 . We have don this studying how does the contour change in the plane $\sigma_8 - \Gamma$ if we fix Ω_m to three different values, and we have seen that the contour does not change much.
- we have checked that using MCMC sampler from Cobaya, we successfully recover the values of these parameters for Uchuu-SDSS lightcones. The recovered values are $\sigma_8 = 0.782^{+0.166}_{-0.183}$, $\Omega_m = 0.302^{+0.106}_{-0.099}$, $H_0 = 75.42^{+25.94}_{-23.29}$, $\Gamma = 0.1769^{+0.0228}_{-0.0208}$ and $S_8 = 0.776^{+0.205}_{-0.208}$.
- We have calculated, then, the contours in $\sigma_8 - \Omega_m$, $\sigma_8 - H_0$ and $H_0 - \Omega_m$ planes for the same confidence levels as mentioned above for SDSS void statistics. The contours obtained for SDSS are much wider than the ones obtained for halo simulation boxes (and Uchuu-SDSS lightcones) because of the huge difference of volume (SDSS volume is approximately 25 times smaller than the three small simulation boxes and 200 times smaller than Uchuu box volume), which means that there are far fewer voids in SDSS than in the boxes and much higher errors. The constrained values we get in this work for SDSS are $\sigma_8 = 1.028^{+0.273}_{-0.305}$, $\Omega_m = 0.296^{+0.110}_{-0.102}$, $H_0 = 83.43^{+29.27}_{-27.20}$, $\Gamma = 0.1947^{+0.0578}_{-0.0516}$ and $S_8 = 1.017^{+0.363}_{-0.359}$. It is important to remark that these constrained values have been obtained supposing that the ratio of Ω_b/Ω_m is constant and given by Planck 2018,
- Next, we have combined our SDSS voids constraints with KiDS-1000, DESY3 and KiDS-1000+DESY3 (Dark Energy Survey and Kilo-Degree Survey Collaboration et al. 2023). The results obtained when combining SDSS voids with KiDS-1000+DESY3 are: $\sigma_8 = 0.858^{+0.040}_{-0.040}$, $\Omega_m = 0.257^{+0.023}_{-0.020}$, $H_0 = 74.17^{+4.66}_{-4.66}$ and $S_8 = 0.794^{+0.016}_{-0.016}$. We can see that when we combine our results with Weak Lensing works, we improve considerably the uncertainties of all the parameters, but H_0 with respect to the uncertainties of only KiDS-1000+DESY3. This is because the confidence level contours in the plane $\sigma_8 - \Omega_m$ obtained in this work and the one from KiDS-1000 are almost orthogonal.
- We have seen that any value of H_0 or Ω_m obtained when combining SDSS voids with the three Weak Lensing works are compatible with Planck 2018 within 1σ (for Ω_m , they are within 2σ , approximately). We have also seen that S_8 value from SDSS voids + DESY3 is compatible with Planck within

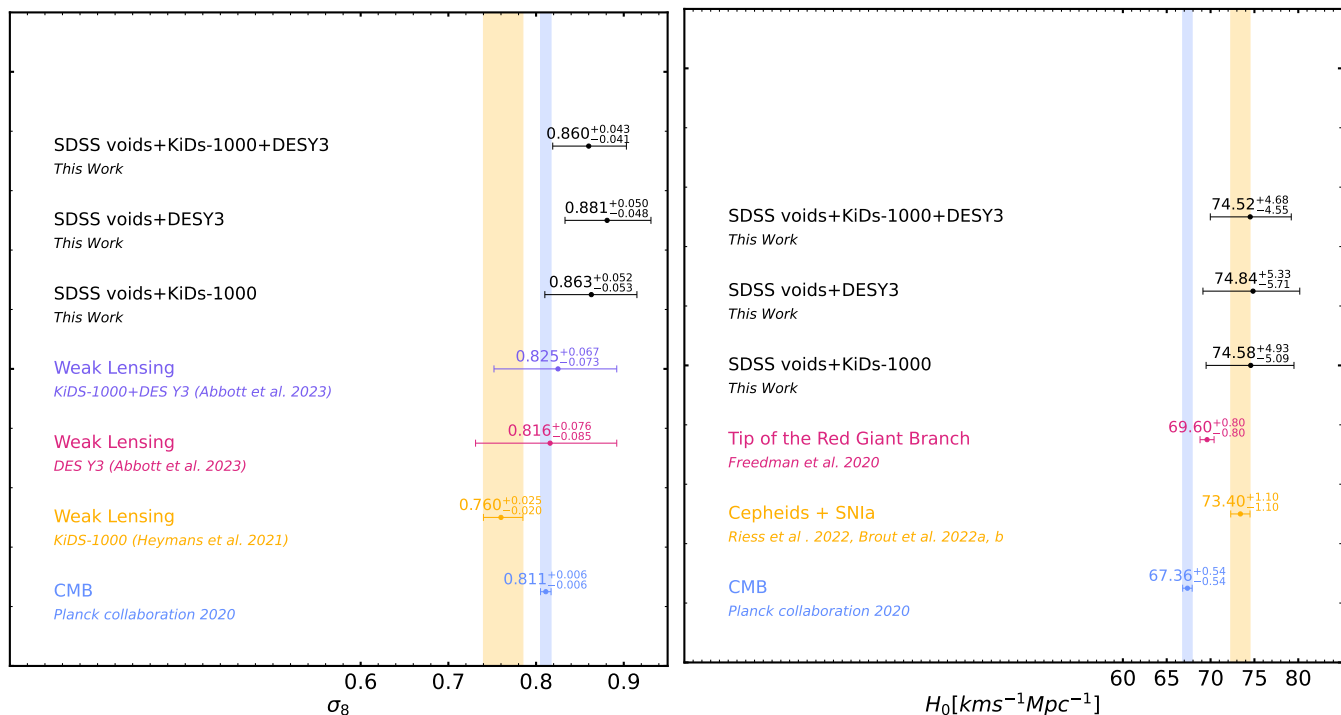


Fig. 12: Comparison between recent constraints on the parameters σ_8 (left panel) and H_0 (right panel) from different cosmological probes. The error bars represent 68% confidence intervals. The black error bars represent the values constrained in this work. The references of the rest of the works, from top to bottom in left panel are: [Dark Energy Survey and Kilo-Degree Survey Collaboration et al. \(2023\)](#), [Heymans, Catherine et al. \(2021\)](#) and [Aghanim et al. \(2020\)](#), and for the right panel: [Freedman et al. \(2020\)](#), [Riess et al. \(2022\)](#), [Brout et al. \(2022a,b\)](#) and [Aghanim et al. \(2020\)](#).

1σ , but SDSS voids + KiDS-1000 and SDSS voids + KiDS-1000 + DESY3 aren't (the former is compatible within 2.7σ and the latter within 2σ).

- Finally, we have compared our results with those obtained in other works where voids are also used in order to constrain the same cosmological parameters that we have constrained in this work, and with parameter constrained via CMB, galaxy clustering, weak lensing and Type Ia Supernova measures. We can check that when combining with Weak Lensing works, we obtain slightly smaller uncertainties than in other works where voids are also used, and when combining with Planck, we obtain much smaller uncertainties. However, if we don't combine our results with any work, our uncertainties are very large because the volume of the samples of Uchuu-SDSS and SDSS used in this work is relatively small in comparison of the volumes of redshift surveys used in other works of voids. For example, in [Contarini et al. \(2024\)](#) BOSS redshift survey is used. If we used this redshift survey, we have predicted that our uncertainties without combining with any work would be very similar to the ones given in [Contarini et al. \(2024\)](#).

Therefore, the most important limitation we face when constraining the cosmological parameters considered in this study is the small volume of the redshift survey sample we have used, which is approximately $\sim 40 \times 10^6 h^{-3} \text{Mpc}^3$. This limitation is expected to be significantly reduced when the Dark Energy Spectroscopic Instrument (DESI) experiment ([DESI Collaboration et al. 2016a,b](#)) is fully available. During its 5 years of operations, DESI will conduct the Bright Galaxy Survey (BGS) of more than 10 million galaxies over the redshift range $0 < z < 0.6$, along with a dark-time redshift survey of 20 million luminous

red galaxies (LRGs), emission-line galaxies (ELGs), and quasars ([Hahn et al. 2023](#)). With an expected footprint of 14000 deg^2 and a longer redshift baseline, DESI will achieve a precision 1–2 orders of magnitude better than that of existing surveys, such as SDSS, BOSS.

In fact, we can estimate how much the errors, considering only void statistics, can decrease with DESI Y1 calculating ratio between the volumes of SDSS and DESI (see Appendix C):

$$\Delta \approx \left(\frac{V_{SDSS}}{V_{BGS,Y1}} \right)^{1/4} \sim \left(\frac{40 \times 10^6 h^{-3} \text{Mpc}^3}{1.2 \times 10^9 h^{-3} \text{Mpc}^3} \right)^{1/4} \sim 0.43 \quad (16)$$

In other words, the uncertainties obtained with the Bright Galaxy Survey from DESI Y1 will be approximately a factor 2 lower than those obtained in this work with the SDSS sample used, and even lower when the full DESI survey is complete. If we additionally combine with other works, then decrease of errors would be larger when increasing the volume of the sample of galaxies used.

Acknowledgements. E. Fernández-García acknowledges financial support from the Severo Ochoa grant CEX2021-001131-S funded by MCIN/AEI/10.13039/501100011033. EFG, FP and AK thanks support from the Spanish MICINN PID2021-126086NB-I00 funding grant. T.I has been supported by IAAR Research Support Program in Chiba University Japan, MEXT/JPSP KAKENHI (Grant Number JP19KK0344, JP21H01122, and JP23H04002), MEXT as “Program for Promoting Researches on the Supercomputer Fugaku” (JPMXP1020200109 and JPMXP1020230406), and JICFuS. We thank Instituto de Astrofísica de Andalucía (IAA-CSIC), Centro de Supercomputación de Galicia (CESGA) and the Spanish academic and research network (RedIRIS) in Spain for hosting Uchuu DR1, DR2 and DR3 in the Skies & Universes site for cosmological simulations. The Uchuu simulations were carried out on Aterui II supercomputer at Center for Computational Astrophysics, CfCA, of National Astronomical Observatory of Japan, and the K computer at the RIKEN Advanced Institute for Computational Science. The Uchuu Data Releases efforts have made

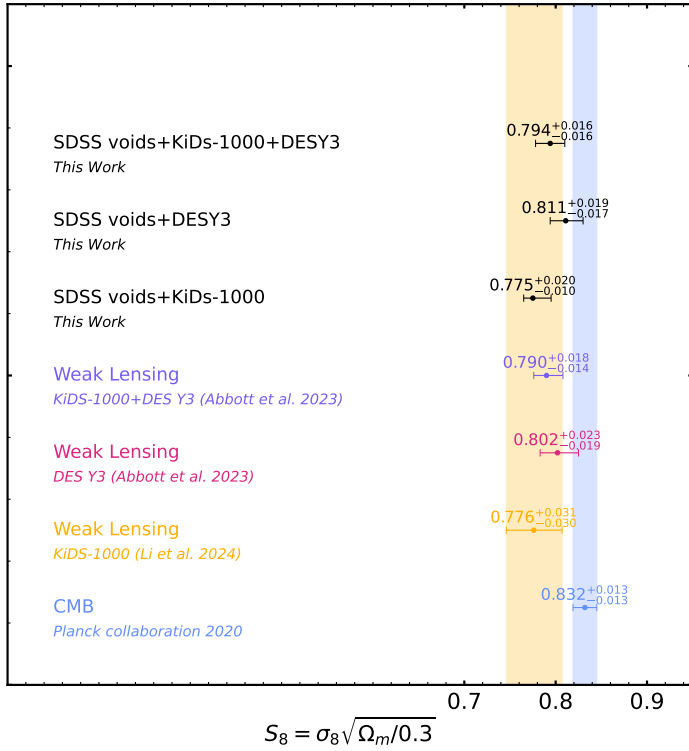


Fig. 13: Comparison between recent constraints on S_8 from different cosmological probes. The error bars represent 68% confidence intervals. The black error bars represent the values constrained in this work. The references of the rest of the works, from top to bottom are: [Dark Energy Survey and Kilo-Degree Survey Collaboration et al. \(2023\)](#), [Li et al. \(2023\)](#), and [Aghanim et al. \(2020\)](#).

use of the skun@IAA_RedIRIS and skun6@IAA computer facilities managed by the IAA-CSIC in Spain (MICINN EU-Feder grant EQC2018-004366-P). The other cosmological simulations were carried out on the supercomputer Fugaku provided by the RIKEN Center for Computational Science (Project ID: hp220173, hp230173, and hp230204). We also thank Joe Zuntz and Anna Porredon for their feedback on our cosmological results. Finally, we are thankful to Peter Taylor for instructing us on the use of CombineHarvesterFlow, for verifying our results and for giving us feedback on the paper.

Data Availability

The Uchuu halo and galaxy boxes and the 4 box catalogs at redshift $z=0.092$, as well as the 32 Uchuu-SDSS galaxy light cones, the SDSS catalogue and the void catalogues from all the previous galaxy and haloes catalogues used in this work are available at: <http://www.skiesanduniverses.org/Simulations/Uchuu/>, together with information on how to read the data and column description. For a list and brief description of the available halo, Uchuu-SDSS and SDSS void catalogues columns, see Appendix E.

References

Abazajian, K. N., Adelman-McCarthy, J. K., Agüeros, M. A., et al. 2009, *ApJS*, 182, 543
 Achitouv, I. 2019, *Physical Review D*, 100
 Aghanim, N., Akrami, Y., Ashdown, M., et al. 2020, *A&A*, 641, A6
 Aikio, J. & Mähönen, P. 1998, *ApJ*, 497, 534
 Aubert, M., Cousinou, M.-C., Escoffier, S., et al. 2022, *MNRAS*, 513, 186
 Aung, H., Nagai, D., Klypin, A., et al. 2023, *MNRAS*, 519, 1648

Bahcall, N. A. 1977, *ARA&A*, 15, 505
 Behroozi, P. S., Wechsler, R. H., & Wu, H.-Y. 2013a, *ApJ*, 762, 109
 Behroozi, P. S., Wechsler, R. H., Wu, H.-Y., et al. 2013b, *ApJ*, 763, 18
 Benson, A. J., Hoyle, F., Torres, F., & Vogeley, M. S. 2003, *MNRAS*, 340, 160
 Betancort-Rijo, J. 1990, *MNRAS*, 246, 608
 Betancort-Rijo, J. 1992, *Phys. Rev. A*, 45, 3447
 Betancort-Rijo, J. & López-Corredoira, M. 2002, *ApJ*, 566, 623
 Betancort-Rijo, J., Patiri, S. G., Prada, F., & Romano, A. E. 2009, *MNRAS*, 400, 1835
 Betancort-Rijo, J. E., Sanchez-Conde, M. A., Prada, F., & Patiri, S. G. 2006, *ApJ*, 649, 579
 Biswas, R., Alizadeh, E., & Wandelt, B. D. 2010, *Phys. Rev. D*, 82, 023002
 Blanton, M. R., Schlegel, D. J., Strauss, M. A., et al. 2005, *AJ*, 129, 2562
 Brout, D., Scolnic, D., Popovic, B., et al. 2022a, *ApJ*, 938, 110
 Brout, D., Taylor, G., Scolnic, D., et al. 2022b, *ApJ*, 938, 111
 Ceccarelli, L., Padilla, N. D., Valotto, C., & Lambas, D. G. 2006, *MNRAS*, 373, 1440–1450
 Chan, H. Y. J., Chiba, M., & Ishiyama, T. 2019, *MNRAS*, 490, 2405
 Chan, K. C., Hamaus, N., & Biagetti, M. 2019, *Physical Review D*, 99
 Chongchitnan, S. & Silk, J. 2010, *ApJ*, 724, 285
 Clampitt, J., Cai, Y.-C., & Li, B. 2013, *MNRAS*, 431, 749–766
 Colberg, J. M., Sheth, R. K., Diaferio, A., Gao, L., & Yoshida, N. 2005, *MNRAS*, 360, 216
 Colless, M., Dalton, G., Maddox, S., et al. 2001, *MNRAS*, 328, 1039
 Colless, M., Peterson, B. A., Jackson, C., et al. 2003, arXiv e-prints, astro
 Contarini, S., Marulli, F., Moscardini, L., et al. 2021, *MNRAS*, 504, 5021
 Contarini, S., Pisani, A., Hamaus, N., et al. 2023, *ApJ*, 953, 46
 Contarini, S., Pisani, A., Hamaus, N., et al. 2024, *A&A*, 682, A20
 Contarini, S., Verza, G., Pisani, A., et al. 2022, *A&A*, 667, A162
 Crocce, M., Pueblas, S., & Scoccimarro, R. 2006, *MNRAS*, 373, 369
 Croton, D. J., Farrar, G. R., Norberg, P., et al. 2005, *MNRAS*, 356, 1155
 Curtis, O., McDonough, B., & Brainerd, T. G. 2024, *ApJ*, 962, A58
 Dark Energy Survey and Kilo-Degree Survey Collaboration, Abbott, T. M. C., Aguena, M., et al. 2023, *The Open Journal of Astrophysics*, 6, 36
 Dawson, K. S., Schlegel, D. J., Ahn, C. P., et al. 2013, *AJ*, 145, 10
 DESI Collaboration, Aghamousa, A., Aguilar, J., et al. 2016a, arXiv e-prints, arXiv:1611.00036
 DESI Collaboration, Aghamousa, A., Aguilar, J., et al. 2016b, arXiv e-prints, arXiv:1611.00037
 Di Valentino, E., Anchordoqui, L. A., Akarsu, O., et al. 2021, *Astroparticle Physics*, 131, 102604
 Dong-Páez, C. A., Smith, A., Szewciw, A. O., et al. 2024, *MNRAS*[arXiv:2208.00540]
 Douglass, K. A., Veyrat, D., & BenZvi, S. 2023, *ApJSupplement Series*, 265, 7
 Einasto, M., Einasto, J., Tago, E., Dalton, G. B., & Andernach, H. 1994, *MNRAS*, 269, 301
 El-Ad, H. & Piran, T. 1997, *ApJ*, 491, 421
 Ereza, J., Prada, F., Klypin, A., et al. 2023, arXiv e-prints, arXiv:2311.14456
 Falck, B., Koyama, K., Zhao, G.-B., & Cautun, M. 2017, *MNRAS*, 475, 3262–3272
 Finelli, F., García-Bellido, J., Kovács, A., Paci, F., & Szapudi, I. 2016, *MNRAS*, 455, 1246
 Freedman, W. L., Madore, B. F., Hoyt, T., et al. 2020, *ApJ*, 891, 57
 Gao, L. & White, S. D. M. 2007, *MNRAS*, 377, L5
 Giovanelli, R. 2010, in *Astronomical Society of the Pacific Conference Series*, Vol. 421, *Galaxies in Isolation: Exploring Nature Versus Nurture*, ed. L. Verdes-Montenegro, A. Del Olmo, & J. Sulentic, 89
 Gkogkou, A., Béthermin, M., Lagache, G., et al. 2023, *A&A*, 670, A16
 Goldwirth, D. S., da Costa, L. N., & van de Weygaert, R. 1995, *MNRAS*, 275, 1185–1194
 Gorski, K. M., Wandelt, B. D., Hansen, F. K., Hivon, E., & Banday, A. J. 1999, arXiv e-prints, astro
 Hahn, C., Wilson, M. J., Ruiz-Macias, O., et al. 2023, *The Astronomical Journal*, 165, 253
 Hamaus, N., Pisani, A., Choi, J.-A., et al. 2020, *J. Cosmology Astropart. Phys.*, 2020, 023
 Hamaus, N., Pisani, A., Sutter, P. M., et al. 2016, *Phys. Rev. Lett.*, 117, 091302
 Hamilton, A. J. S. 1998, in *Astrophysics and Space Science Library* (Springer Netherlands), 185–275
 Heymans, Catherine, Tröster, Tilman, Asgari, Marika, et al. 2021, *A&A*, 646, A140
 Hoffman, Y., Metuki, O., Yepes, G., et al. 2012, *MNRAS*, 425, 2049
 Hoffman, Y. & Shaham, J. 1982, *ApJ*, 262, L23
 Holder, G., Haiman, Z., & Mohr, J. J. 2001, *ApJ*, 560, L111
 Hoyle, F. & Vogeley, M. S. 2002, *ApJ*, 566, 641
 Ishiyama, T., Fukushige, T., & Makino, J. 2009, *Publications of the Astronomical Society of Japan*, 61, 1319
 Ishiyama, T., Nitadori, K., & Makino, J. 2012
 Ishiyama, T., Prada, F., Klypin, A. A., et al. 2021, *MNRAS*, 506, 4210
 Jennings, E., Li, Y., & Hu, W. 2013, *MNRAS*, 434, 2167

- Kaiser, N. 1987, MNRAS, 227, 1
- Kiang, T. & Saslaw, W. C. 1969, MNRAS, 143, 129
- Lavaux, G. & Wandelt, B. D. 2010, MNRAS, 403, 1392
- Layzer, D. 1954, AJ, 59, 268
- Lee, J. & Park, D. 2009, ApJ, 696, L10
- Li, B., Zhao, G.-B., & Koyama, K. 2012, MNRAS, 421, 3481
- Li, C., Kauffmann, G., Jing, Y. P., et al. 2006, MNRAS, 368, 21
- Li, S.-S., Hoekstra, H., Kuijken, K., et al. 2023, A&A, 679, A133
- Little, B. & Weinberg, D. H. 1994, MNRAS, 267, 605–628
- Martino, M. C. & Sheth, R. K. 2009, arXiv e-prints, arXiv:0911.1829
- Mauland, R., Elgarøy, O., Mota, D. F., & Winther, H. A. 2023, A&A, 674, A185
- Mo, H. J. & White, S. D. M. 1996, MNRAS, 282, 347
- Nadathur, S. 2016, MNRAS, 461, 358
- Oogi, T., Ishiyama, T., Prada, F., et al. 2023, MNRAS, 525, 3879
- Patiri, S. G., Betancort-Rijo, J., & Prada, F. 2006a, MNRAS, 368, 1132
- Patiri, S. G., Betancort-Rijo, J., & Prada, F. 2012, A&A, 541, L4
- Patiri, S. G., Betancort-Rijo, J. E., Prada, F., Klypin, A., & Gottlöber, S. 2006b, MNRAS, 369, 335
- Perico, E. L. D., Voivodic, R., Lima, M., & Mota, D. F. 2019, A&A, 632, A52
- Planck Collaboration, Ade, P. A. R., Aghanim, N., et al. 2016, A&A, 594, A13
- Prada, F., Behroozi, P., Ishiyama, T., Klypin, A., & Pérez, E. 2023, arXiv e-prints, arXiv:2304.11911
- Press, W. H. & Schechter, P. 1974, ApJ, 187, 425
- Reid, B., Ho, S., Padmanabhan, N., et al. 2015, MNRAS, 455, 1553
- Riess, A. G., Yuan, W., Macri, L. M., et al. 2022, ApJ, 934, L7
- Rodríguez-Medrano, A. M., Springel, V., Stasyszyn, F. A., & Paz, D. J. 2024, MNRAS, 528, 2822
- Rubiño-Martín, J. A., Betancort-Rijo, J., & Patiri, S. G. 2008, MNRAS, 386, 2181
- Ryden, B. S. 1995, ApJ, 452, 25
- Sahlén, M., Zubeldía, I., & Silk, J. 2016, ApJLetters, 820, L7
- Sheth, R. K. & Tormen, G. 2002, MNRAS, 329, 61
- Sheth, R. K. & Van De Weygaert, R. 2004, MNRAS, 350, 517
- Song, H. & Lee, J. 2009, ApJ, 701, L25
- Sutter, P. M., Lavaux, G., Hamaus, N., et al. 2014, MNRAS, 442, 462
- Swanson, M. E. C., Tegmark, M., Hamilton, A. J. S., & Hill, J. C. 2008, MNRAS, 387, 1391
- Taylor, P. L., Cuceu, A., To, C.-H., & Zaborowski, E. A. 2024, arXiv e-prints, arXiv:2406.06687
- Tikhonov, A. V. 2006, Astronomy Letters, 32, 727–733
- Tikhonov, A. V. 2007, Astronomy Letters, 33, 499–511
- Torrado, J. & Lewis, A. 2019, Cobaya: Bayesian analysis in cosmology, Astrophysics Source Code Library, record ascl:1910.019
- Torrado, J. & Lewis, A. 2021, J. Cosmology Astropart. Phys., 2021, 057
- van de Weygaert, R. & Sheth, R. 2003, arXiv e-prints, astro
- Voivodic, R., Lima, M., Llinares, C., & Mota, D. F. 2017, Physical Review D, 95
- von Benda-Beckmann, A. M. & Mueller, V. 2007, arXiv e-prints, arXiv:0710.2783
- White, S. D. M. 1979, MNRAS, 186, 145
- Woodfinden, A., Percival, W. J., Nadathur, S., et al. 2023, MNRAS, 523, 6360
- Yang, X., Mo, H. J., van den Bosch, F. C., & Jing, Y. P. 2005, MNRAS, 357, 608
- York, D. G., Adelman, J., Anderson, John E., J., et al. 2000, AJ, 120, 1579
- Zeldovich, I. B., Einasto, J., & Shandarin, S. F. 1982, Nature, 300, 407
- Zentner, A. R., Hearin, A., van den Bosch, F. C., Lange, J. U., & Villarreal, A. S. 2019, MNRAS, 485, 1196
- Zhao, C., Tao, C., Liang, Y., Kitaura, F.-S., & Chuang, C.-H. 2016, MNRAS, 459, 2670
- Zuntz, J., Paterno, M., Jennings, E., et al. 2015, Astronomy and Computing, 12, 45–59

Appendix A: Void statistics theoretical framework in detail

In this Appendix we explicitly write all necessary quantities in order to calculate $P_0(r)$ (VPF) and $\bar{n}_v(r)$ in real and redshift space. This theoretical framework can also be consulted in [Betancort-Rijo et al. \(2009\)](#).

Real space

The first step to calculate all the terms that appear in equation (2) is to develop equation (5). In [Patiri et al. \(2006a\)](#), it is shown that for dark matter haloes, u can be written as

$$u = [\bar{n}V(1 + \delta)][1 + \delta_{ns}] \quad (\text{A.1})$$

where \bar{n} denotes the mean number density of those haloes in the sample (usually haloes larger than some given mass), V is the volume of the sphere and δ the actual enclosed density contrast within the sphere. The first factor on the right-hand side of the equation is the integral of the probability density within the sphere for haloes tracing the mass (i.e. no bias, which is true in the very low mass limit). In general, haloes are biased tracers of the underlying mass distribution, due to the initial clustering of the protohaloes before they move along with mass (i.e., statistical clustering). The second term of the equation accounts for this biasing. In [Patiri et al. \(2006a\)](#) an approximation for this bias is obtained as a function of the linear enclosed density contrast within the sphere (δ_l):

$$1 + \delta_{ns}(\delta_l) = A(m)e^{-b(m)\delta_l^2} \quad \forall \quad \delta_l \leq -1 \quad (\text{A.2})$$

where $A(m)$, $b(m)$ are coefficients mainly depending on the halo mass. In [Patiri et al. \(2006a\)](#) is demonstrated that, using Zeldovich approximation, $P_n(r)$ can be rewritten as

$$P_n(r) = \int_{-\infty}^{1.6} P(\delta_l, r) \frac{[u(\delta_l)]^n}{n!} e^{-u(\delta_l)} d\delta_l \quad (\text{A.3})$$

where $u(\delta_l)$ is now a function of δ_l through the dependence of the actual density contrast, δ , on its linear counterpart, δ_l :

$$u(\delta_l) = (\bar{n}V[1 + \delta(\delta_l, r)])(1 + \delta_{ns}(\delta_l)) \quad (\text{A.4})$$

$\delta(\delta_l, r)$ is basically the relationship between the actual and the linear density contrast within a sphere as given by the standard spherical collapse model, except for a small correcting term depending on r .

Doing some manipulation, $P_n(r)$ can be rewritten as

$$P_n(r) = \frac{1}{n!} \int_{-7}^0 P(\delta_l, r) [u(\delta_l)]^n e^{-u(\delta_l)} d\delta_l \quad (\text{A.5})$$

where $u(\delta_l)$ is now

$$u(\delta_l) = \bar{n}V[1 + DELF(\delta_l, r)]Ae^{-b\delta_l^2} \quad (\text{A.6})$$

DELF is a function of δ_l and r that gives the mean actual density contrast within a sphere with radius r with enclosed linear density contrast δ_l :

$$DELF(\delta_l, r) =$$

$$\frac{1 + DELT(\delta_l)}{[1 - (4/21)[1 + DELT(\delta_l)]^{2/3}[\sigma(r[1 + DELT(\delta_l)]^{1/3})]^2]} \quad (\text{A.7})$$

where $DELT(\delta_l)$ denotes the relationship between the actual and linear enclosed density contrasts in the spherical collapse model ([Patiri et al. 2006a](#)):

$$1 + DELT(\delta_l) \approx (1 - 0.607\delta_l)^{-1.66} \quad (\text{A.8})$$

$\sigma(Q)$ is the rms of the linear density contrast on a sphere with Lagrangian radius Q . In this equation, $\sigma(Q)$ is evaluated at $Q = r[1 + DELT(\delta_l)]^{1/3}$. A , b in equation (A.6) are also functions of δ_l given by (see [Rubiño-Martín et al. 2008](#), for more details)

$$A = A(m, Q = r[1 + DELT(\delta_l)]^{1/3}) \times \left[\frac{D(z)\sigma_8}{0.9} \right]^{0.88} \left(\frac{\Gamma}{0.21} \right)^{0.174} \quad (\text{A.9})$$

$$B = B(m, Q = r[1 + DELT(\delta_l)]^{1/3}) \times \left[\frac{D(z)\sigma_8}{0.9} \right]^{-2.55} \left(\frac{\Gamma}{0.21} \right)^{-0.82} \quad (\text{A.10})$$

where $A(m, Q)$, $b(m, Q)$ are functions of the mass of the objects and the Lagrangian radius of the regions being considered:

$$A(m, Q) = \left[1.577 - 0.298 \left(\frac{Q}{8} \right) \right] - \left[0.0557 + 0.00447 \left(\frac{Q}{8} \right) \right] \ln m - \left[0.00565 + 0.0018 \left(\frac{Q}{8} \right) \right] [\ln m]^2 \quad (\text{A.11})$$

$$b(m, Q) = \left[0.0025 - 0.00146 \left(\frac{Q}{8} \right) \right] + \left[0.121 - 0.0156 \left(\frac{Q}{8} \right) \right] m^{0.335+0.019Q/8} \quad (\text{A.12})$$

$$m = \frac{M}{3.4866 \times 10^{11} h^{-1} M_\odot} \left(\frac{0.3}{\Omega_m} \right) \quad (\text{A.13})$$

where $D(z)$ is the linear growth factor normalized to be 1 at present and M is the mass of the objects. M is the minimum mass of distinct haloes in the sample with halo number density equal to \bar{n}_{sample} , with this number density containing only distinct haloes. If our sample contains subhaloes, too, then the mass we have to use is M_g .

It is important to remark that equations (A.9) and (A.10) are only valid for $z = 0$. If we want to calculate this functions in a different redshift, then we have to make the following change:

$$\sigma_8 \rightarrow \sigma_8 \frac{D(z)}{D(z=0)} \quad (\text{A.14})$$

where $D(z)$ is the linear growth factor of density fluctuations in the model under consideration.

We already have all terms in order to calculate $u(\delta_l)$ from equation (A.5), so all we need now is to calculate $P(\delta_l, r)$, which is the probability function of the linear density contrast within an Eulerian space, and can be calculated as (Betancort-Rijo & López-Corredoira 2002):

$$P(\delta_l, r) = \frac{\exp[(-1/2)\delta_l^2/(\sigma(r[1 + DELF(\delta_l, r)]^{1/3}))^2]}{\sqrt{2\pi}} \times [1 + DELF(\delta_l, r)]^{-[1-(\alpha/2)]} \times \frac{d}{d\delta_l} \left(\frac{\delta_l}{\sigma(r[1 + DELF(\delta_l, r)]^{1/3})} \right) \quad (\text{A.15})$$

where

$$\alpha(\delta_l, r) = 0.54 + 0.173 \ln \left(\frac{r[1 + DELF(\delta_l, r)]^{1/3}}{10} \right) \quad (\text{A.16})$$

and

$$\sigma(Q) = \sigma(Q, \Gamma) \approx \sigma_8 A(\Gamma) Q^{-B(\Gamma) - C(\Gamma)Q} \quad (\text{A.17})$$

$$A(\Gamma) = 2.01 + 3.9\Gamma \quad (\text{A.18})$$

$$B(\Gamma) = 0.2206 + 0.361\Gamma^{1.5} \quad (\text{A.19})$$

$$C(\Gamma) = 0.182 + 0.0411 \ln \Gamma \quad (\text{A.20})$$

This fit is valid for $Q \geq 3h^{-1}\text{Mpc}$ and $0.1 \geq \Gamma \geq 0.5$.

Redshift space

The theoretical framework developed above is only valid for voids in real space. However, if we want to constrain σ_8 using surveys such as SDSS, this surveys provide galaxy positions in redshift space. In this space (redshift space), the peculiar velocity of the galaxies is added to the velocity expansion of the Universe. This generates some distortions which result in elongated structures known as *Fingers of God* (see Hamilton (1998) for more details).

If we want to calculate $\bar{n}_v(r)$ and $P_n(r)$ in redshift space instead of real space, all we have to do is change r by:

$$r = r^* \times \{1 + gVEL[\delta]\}^{-1/3} \quad (\text{A.21})$$

where r is the radius of a sphere in real space and r^* is the radius of that sphere in redshift space. Additionally, it has been found comparing the average outflow around the relevant voids with that given by the spherical expansion model that the value of g is around 0.85. This is also the value that provide the best agreement with simulations.

VEL(δ) is defined so that the peculiar velocity V , of mass element at distance r from the centre of a spherical mass concentration (or defect) enclosing actual density contrast δ is given by

$$V = HrVEL(\delta) \quad (\text{A.22})$$

where H is the Hubble constant at the time being considered. In Betancort-Rijo et al. (2006) it is shown that

$$VEL(\delta) = -\frac{1}{3} \frac{d \ln D(a)}{d \ln a} \frac{DELK(\delta)}{1 + \delta} \left(\frac{d}{d\delta} DELK(\delta) \right)^{-1} \quad (\text{A.23})$$

where $D(a)$ is the growth factor as a function of the expansion factor, a , and $DELK(\delta)$ is the inverse function of $DELK(\delta_l)$ (see Mo & White 1996; Sheth & Tormen 2002):

$$DELK(\delta) = \frac{\delta_c}{1.68647} \left(1.68647 - \frac{1.35}{(1 + \delta)^{2/3}} - \frac{1.12431}{(1 + \delta)^{1/2}} + \frac{0.78785}{(1 + \delta)^{0.58661}} \right) \quad (\text{A.24})$$

where δ_c is the linear density contrast for spherical collapse model, which for the concordance cosmology at present is 1.676.

Finally, the expression of $\frac{d \ln D(a)}{d \ln a}$ is:

$$\frac{d \ln D(a)}{d \ln a} \approx 1.06 \left(\frac{(1 + z)^3}{[(1 + z)^3 + \Omega_\Lambda / \Omega_m]} \right)^{0.6} \quad (\text{A.25})$$

In Table B.2 the values of VPF predicted by theoretical framework and obtained through the four halo simulation boxes are shown. It can be checked that theoretical framework predicts an increase of $P_0(r)$ when going from real to redshift space, as it happens in simulations.

Appendix B: Comparison of voids statistics in the distribution of haloes and galaxies in mocks with theoretical framework

In this Appendix, we show the results obtained with the theoretical framework presented in Appendix A and compare it with the results of the halo and galaxy simulation boxes. We do this in real and redshift space. We also check if we recover the values of σ_8 and Γ using the theoretical framework with Maximum Likelihood test with Bayesian approach.

Appendix B.1: Real Space

Statistics of voids obtained in halo simulation boxes and predicted by theoretical framework in real space have already been discussed in Section 4. Here, we briefly summarize the most important results obtained and present the constraints achieved of σ_8 and Γ . This is a crucial step to take to check that the theoretical framework works correctly, as it is essential to recover the real values of σ_8 and Γ of each simulation.

In Table B.1 the values of $P_0(r)$ obtained with theoretical framework and simulations can be seen. The results are represented in Figure 5. As we have already seen in Section 4, the dependence of the VPF predicted by theoretical framework is the same as that shown by simulations, and all values with $r > 12h^{-1}\text{Mpc}$ are within 10% of the ratio between simulations and theoretical framework, being compatible with unity those with $r > 14h^{-1}\text{Mpc}$.

In Figure 6, we can see the number density of voids larger than r for the four halo simulation boxes. As we have already seen, the agreement between theoretical framework and simulation values is good, specially for intermediate radius bins (i.e. r between 12 and 18 $h^{-1}\text{Mpc}$).

Therefore, we are now in the position to use the theoretical framework and simulations to constrain σ_8 and H_0 (we fix in each case Ω_m to the real value of each simulation box) and obtain the confidence contours using maximum likelihood test and the standard Bayesian approach. This can be seen in the first column of Figure B.1. In this Figure, we can see that all real values (black points) are inside the 1σ contour.

Therefore, we successfully recover the values of σ_8 and Γ of the simulations with the theoretical framework, and we can take one more step to do this study in redshift space.

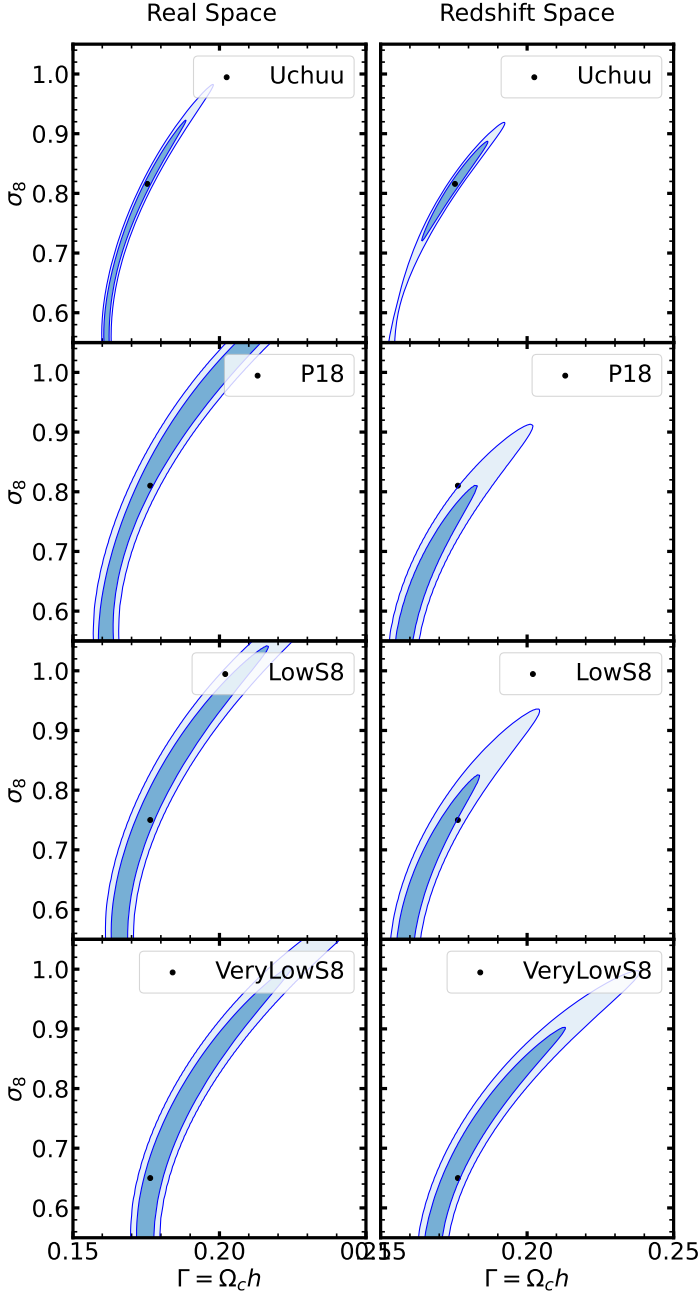


Fig. B.1: Constraints from $N_{v,i}$ identified in Uchuu (first row), P18 (second row), Low (third row) and VeryLow (row) halo simulation boxes in real (first column) and redshift (second column) spaces using Maximum Likelihood test. The contours indicate the 68% (1σ) and 95% (2σ) confidence levels. The black dots are the real values of σ_8 and H_0 of each simulation.

Appendix B.2: Redshift Space

Now we can move to redshift space and check if our model to transform distances from real to redshift space (i.e. equation (A.21)) is accurate enough.

In the upper panel of Figure B.2 we can observe the VPF (multiplied by r^{10} to distinguish more easily each simulation for large radii) obtained by theoretical framework (continuous lines) and simulations (dots), and in Table B.2 we can see the numerical values. In the bottom panel of the same Figure, the ratio between simulations and theoretical framework is shown. Again, taking into account the errors, the agreement between theoretical framework and simulations is good.

In the upper panel of Figure B.3 we can see the $\bar{n}_v(r)$. In the bottom panel of the same Figure, the ratio between simulations and theoretical framework is shown. The agreement between simulations and theoretical framework is good, too, although there are big oscillations for large radius $r > 20h^{-1}$ which make theoretical framework not to be compatible with simulations. This can be due to not having enough statistics for these radius bins.

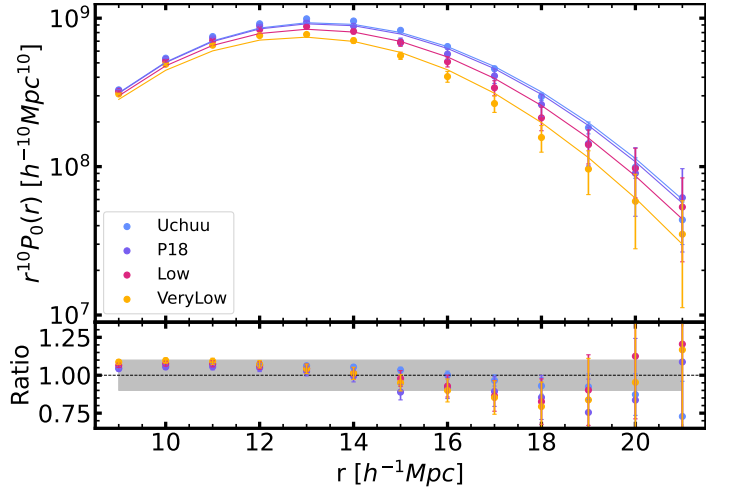


Fig. B.2: In top panel the VPF in redshift space is shown for the theoretical framework (lines) and simulations (dots), while the ratio between simulations and theoretical framework is shown in bottom panels for the Uchuu, P18, Low and VeryLow box catalogs with number density $\bar{n} = 3 \times 10^{-3} h^{-3} \text{Mpc}^3$. Shaded region in bottom panel indicates delimits the region between 0.9 and 1.10 for the ratio.

The contours obtained with maximum likelihood test for the halo simulation boxes in redshift space can be seen in the second column of Figure B.1. In that Figure, we can see that we obtain a small contour for Uchuu in redshift space, unlike in real space. Additionally, we recover Planck 2018 values of σ_8 and H_0 within 1σ for the P18 box catalog, and within 2σ for Low and VeryLow. Therefore, in redshift space we don't successfully recover the real values of the parameters in simulations within 1σ as we do in real space. This can be due to the transformation we have used in order to transform the theoretical framework from real to redshift space (see equation (A.21)). However, we can recover the real values withing 2σ for the four halo simulation boxes.

Appendix C: Scaling of errors with volume

An important study that must be made is the scaling of errors with the volume of the samples used, i.e., how much do errors

r	$P_{0,Uchuu}^{th}$	$P_{0,Uchuu}^{sim}$	$P_{0,P118}^{th}$	$P_{0,P118}^{sim}$	$P_{0,Low}^{th}$	$P_{0,Low}^{sim}$	$P_{0,VeryLow}^{th}$	$P_{0,VeryLow}^{sim}$
9	7.216	7.782	7.163	7.703	6.936	7.520	6.682	7.250
10	3.847	4.176	3.810	4.097	3.659	3.966	3.485	3.762
11	1.946	2.106	1.922	2.044	1.829	1.955	1.719	1.821
12	0.9340	0.9980	0.9194	0.9547	0.8659	0.9023	0.8015	0.8179
13	0.4251	0.4452	0.4169	0.4206	0.3881	0.3889	0.3530	0.3455
14	0.1833	0.1884	0.1790	0.1722	0.1645	0.1556	0.1467	0.1399
15	0.07484	0.07423	0.07277	0.06674	0.06586	0.05914	0.05743	0.04977
16	0.02891	0.02775	0.02797	0.02448	0.02489	0.02032	0.02116	0.01721
17	0.01055	9.863×10^{-3}	0.01015	8.260×10^{-3}	8.872×10^{-3}	6.640×10^{-3}	7.331×10^{-3}	5.540×10^{-3}
18	3.638×10^{-3}	3.421×10^{-3}	3.479×10^{-3}	2.940×10^{-3}	2.979×10^{-3}	2.410×10^{-3}	2.385×10^{-3}	1.800×10^{-3}
19	1.183×10^{-3}	1.017×10^{-3}	1.124×10^{-3}	1.180×10^{-3}	9.412×10^{-4}	9.500×10^{-4}	7.276×10^{-4}	5.800×10^{-4}
20	2.628×10^{-4}	2.958×10^{-4}	3.422×10^{-3}	4.800×10^{-4}	2.796×10^{-4}	3.800×10^{-4}	2.080×10^{-4}	1.800×10^{-4}
21	1.048×10^{-4}	1.125×10^{-4}	9.804×10^{-5}	1.700×10^{-4}	7.801×10^{-5}	1.600×10^{-4}	5.567×10^{-5}	1.100×10^{-4}

Table B.1: Values of VPF for simulations (P_0^{sim}) and theoretical framework for the four halo simulation boxes with number (halo) density $\bar{n} = 3 \times 10^{-3} h^3 \text{Mpc}^{-3}$ and snapshot $z \approx 0.1$ in real space. All values are in units of 10^{-2} .

r	$P_{0,Uchuu}^{th}$	$P_{0,Uchuu}^{sim}$	$P_{0,P118}^{th}$	$P_{0,P118}^{sim}$	$P_{0,Low}^{th}$	$P_{0,Low}^{sim}$	$P_{0,VeryLow}^{th}$	$P_{0,VeryLow}^{sim}$
9	9.059	9.440	8.999	9.333	8.643	9.151	8.181	8.842
10	5.099	5.379	5.054	5.291	4.810	5.139	4.490	4.888
11	2.737	2.901	2.707	2.832	2.550	2.718	2.344	2.535
12	1.402	1.482	1.383	1.434	1.288	1.355	1.163	1.233
13	0.6848	0.7187	0.6732	0.6817	0.6192	0.6376	0.5481	0.5635
14	0.3189	0.3310	0.3124	0.3060	0.2833	0.2820	0.2452	0.2442
15	0.1414	0.1437	0.1380	0.1205	0.1232	0.1184	0.1040	0.09690
16	0.05973	0.05862	0.05803	0.05212	0.05091	0.04628	0.04177	0.03675
17	0.02400	0.0264	0.02320	0.2025	0.01997	0.01684	0.01588	0.01320
18	9.164×10^{-3}	8.300×10^{-3}	8.815×10^{-3}	7.33×10^{-3}	7.426×10^{-3}	5.970×10^{-3}	5.706×10^{-3}	4.400×10^{-3}
19	3.324×10^{-3}	2.983×10^{-3}	3.179×10^{-3}	2.330×10^{-3}	2.617×10^{-3}	2.290×10^{-3}	1.936×10^{-3}	1.570×10^{-3}
20	1.145×10^{-3}	9.667×10^{-4}	1.088×10^{-4}	8.800×10^{-4}	8.735×10^{-4}	9.500×10^{-4}	6.201×10^{-4}	5.700×10^{-4}
21	3.738×10^{-4}	2.625×10^{-4}	3.529×10^{-4}	3.700×10^{-4}	2.758×10^{-4}	3.200×10^{-4}	1.872×10^{-5}	2.100×10^{-4}

Table B.2: Values of VPF in redshift space for simulations (P_0^{sim}) and theoretical framework (P_0^{th}) for the four halo simulation boxes with number (halo) density $\bar{n} = 3 \times 10^{-3} h^3 \text{Mpc}^{-3}$ and snapshot $z \approx 0.1$. All values are in units of 10^{-2} .

decrease when the volume of the sample is increased. From Figure C.1 it is evident that the confidence level contours (and, therefore, the constrained values of each parameter) decrease considerably when we consider a sample with a larger volume. In addition, we can see that the confidence level contour size of a single random Uchuu-SDSS lightcone voids is similar to the one obtained for SDSS voids.

In Table C.1 we can see the constrained values for Uchuu-SDSS void and SDSS voids, and the ratio of the SDSS voids and Uchuu-SDSS voids. This ratio has been calculated as the mean value between the ratios of the upper and lower errors (for example, for the first row, $0.5 [(0.264/0.167) + (0.295/0.187)] = 1.58$). It can be seen that we obtain similar values of the ratio for Ω_m and H_0 . We can also see that the ratios for σ_8 and Γ (the fundamental parameters of the theoretical framework) are very far from $\sqrt{32} \sim 5.66$, but they are closer to $32^{1/4} \sim 2.38$. Therefore, we can predict that the scaling of the errors with the volume of the samples is very similar to $\sim V^{-1/4}$, with V being the ratio of the volumes of the two samples.

	Uchuu-SDSS voids	SDSS voids	Ratio
σ_8	$0.793^{+0.167}_{-0.187}$	$1.044^{+0.263}_{-0.295}$	1.58
Ω_m	$0.305^{+0.106}_{-0.099}$	$0.298^{+0.118}_{-0.105}$	1.09
H_0	$75.29^{+26.92}_{-22.57}$	$84.43^{+30.52}_{-29.06}$	1.21
Γ	$0.1787^{+0.0237}_{-0.0217}$	$0.1981^{+0.0532}_{-0.0567}$	2.43
S_8	$0.792^{+0.211}_{-0.213}$	$1.036^{+0.358}_{-0.350}$	1.67

Table C.1: Constraints of σ_8 , Ω_m , H_0 (in units of $\text{kms}^{-1} \text{Mpc}^{-1}$), $S_8 = \sigma_8 \sqrt{\Omega_m/0.3}$ and $\Gamma = \Omega_c h$ for Uchuu-SDSS voids (first column), SDSS voids (second column) and the mean value of the ratio of SDSS and Uchuu-SDSS 68% uncertainties.

Appendix D: Theoretical framework with different number densities of galaxies

In this work, we have constrained the parameters σ_8 , Ω_m and H_0 using galaxy samples with a number density of $3 \times 10^{-3} h^{-3} \text{Mpc}^3$ at a redshift of $z \sim 0.1$. We have verified that the theoretical framework successfully predicts both the Void Probability Function and the number density of voids larger than r for this number density. However, it remains to be checked whether the the-

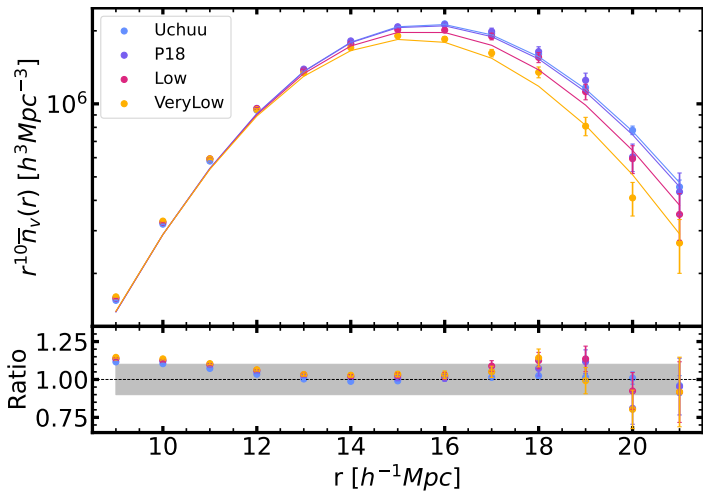


Fig. B.3: In top panel the number density of voids larger than r in redshift space is shown for the theoretical framework (lines) and simulations (dots), while the ratio between simulations and theoretical framework is shown in bottom panels for the Uchuu, P18, Low and VeryLow box catalogs with number density $\bar{n} = 3 \times 10^{-3} h^{-3} \text{Mpc}^3$. Shaded region in bottom panel indicates delimits the region between 0.9 and 1.10 for the ratio.

that must be changed for each sample is the mass, m_g . The number densities we use are $n_g = \{1 \times 10^{-3}, 2 \times 10^{-3}, 3 \times 10^{-3}, 4 \times 10^{-3}, 5 \times 10^{-3}, 6 \times 10^{-3}\} h^{-3} \text{Mpc}^3$.

In Figure D.1 we can observe the VPF (left panel) and number density of voids larger than r (right panel) predicted by the theoretical framework with continuous lines and obtained in Uchuu galaxy simulation boxes for these galaxy number densities with dots and the abundance of voids larger than r (right panel). It can be seen that the theoretical framework predicts successfully the VPF for all galaxy number densities without any need to change the values of α or μ , except for galaxy number densities smaller than $n_g \leq 2 \times 10^{-3} h^{-3} \text{Mpc}^3$. Therefore, the theoretical framework is only valid for large galaxy number densities ($n_g \geq 3 \times 10^{-3} h^{-3} \text{Mpc}^3$), and the coefficients α and μ depend on this galaxy number density.

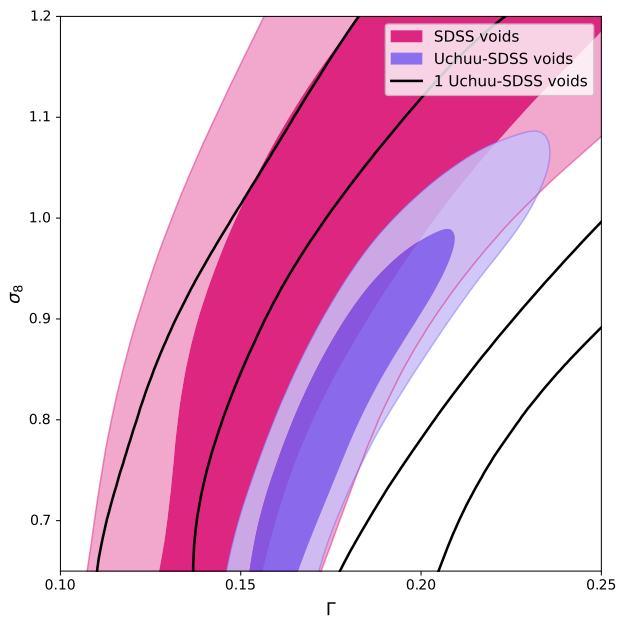


Fig. C.1: Void Probability Function (left panel) and number density of voids larger than r (right panel) predicted by the theoretical framework developed in this work (continuous lines) and measured in Uchuu galaxy box (points) for different galaxy number densities, n_g , at redshift $z = 0.092$.

oretical framework continues to successfully predict these two statistics at a different number densities of galaxies.

In order to check if the theoretical framework works correctly for different number densities of galaxies we need to construct different samples (from Uchuu galaxy simulation box, for example) with different galaxy number densities, calculate the VPF and $n_v(r)$ from that sample and compare with the predicted value given by the theoretical framework with the same coefficients that we have calculated in this work. The only parameter

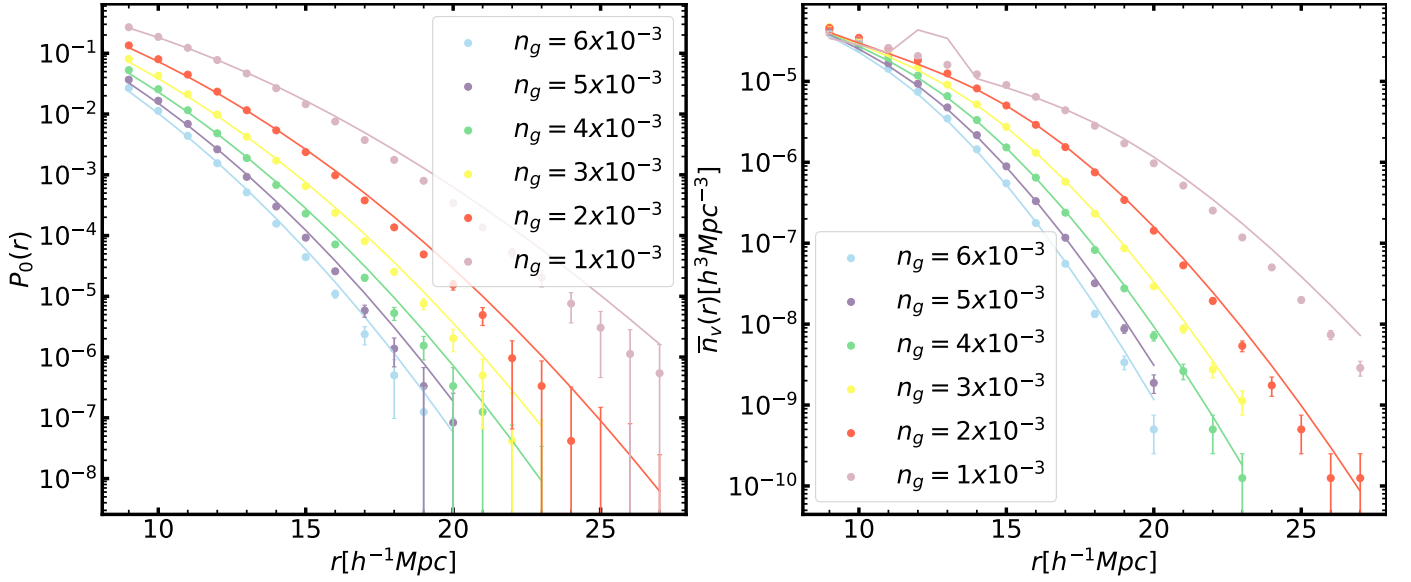


Fig. D.1: Void Probability Function (left panel) and number density of voids larger than r (right panel) in real space predicted by the theoretical framework developed in this work (continuous lines) and measured in Uchuu galaxy box (points) for different galaxy number densities, n_g , at redshift $z = 0.092$.

Appendix E: Content of the void catalogues used in this work

The columns of the void catalogues of halo and galaxy simulation boxes are the following

- X[MPC/H]: x-position of the centre of the void (comoving h^{-1} Mpc).
- Y[MPC/H]: y-position of the centre of the void (comoving h^{-1} Mpc).
- Z[MPC/H]: z-position of the centre of the void (comoving h^{-1} Mpc).
- RADIUS[MPC/H]: radius of the void (comoving h^{-1} Mpc)

For Uchuu-SDSS lightcones and SDSS, there are four additional columns:

- RA[DEG]: right ascension (degrees)
- DEC[DEG]: declination (degrees).
- ZOBS: observed redshift of the centre of the void (accounting for peculiar velocities. The fiducial cosmology used for SDSS voids is Planck 2015 (Planck Collaboration et al. 2016)).
- completeness: mean completeness of the void, calculated as the mean completeness of all the points uniformly distributed in its volume.